Ambient ZeroScatter: Ambient BPSK and QPSK Backscatter Communication using Existing Digital I/O Pins

Anissa Dadkhah

A thesis
submitted in partial fulfillment of the
requirements for the degree of

Master of Science in Electrical Engineering

University of Washington

2019

Committee:

Matthew S. Reynolds, Chair

Arka Majumdar

Program Authorized to Offer Degree:
Department of Electrical & Computer Engineering

University of Washington

Abstract

Ambient ZeroScatter: Ambient BPSK and QPSK Backscatter Communication using Existing Digital I/O Pins

Anissa Dadkhah

Chair of the Supervisory Committee:
Professor Matthew S. Reynolds
Department of Electrical & Computer Engineering

ZeroScatter is an ultra-low-cost, minimum-complexity approach that enables backscatter wireless data uplink from billions of existing, commodity microcontrollers (MCUs) and field-programmable gate arrays (FPGAs). Existing MCU and FPGA based backscatter wireless sensors rely on external components such as RF FETs, PIN diodes, or varactors to perform the backscatter modulation function. We demonstrate that completely unmodified digital I/O pins on MCUs and FPGAs can be re-purposed as binary phase-shift keying (BPSK) backscatter modulators in the UHF and microwave bands with zero added components, and that multiple digital I/O pins can be used in combination with series or shunt impedances to produce quadrature phase-shift keying (QPSK) backscatter modulation. We additionally demonstrate a complete ambient backscatter communication system, consisting of the BPSK ZeroScatter tag, dipole antennas, and a direct sampling digital receiver. With an input clock frequency of 2.9 Gsps, the resolution of the receiver's analog-to-digital converter (ADC) is 14 bits and the effective number of bits (ENOB) is 9 bits. By leveraging RF signals already present in the environment, ambient backscatter does not require a dedicated carrier source as in traditional backscatter communication. The ambient ZeroScatter system uses ambient digital television (DTV) signals as the carrier source, enabling the ZeroScatter tag to transmit sensor data via backscatter. The data is then received and processed by the digital receiver.

TABLE OF CONTENTS

LIST OF FIGURES

ACKNOWLEDGMENTS

The author wishes to express sincere appreciation to her advisor, Professor Matt Reynolds, and fellow lab members James Rosenthal, Claire Watts, Apoorva Sharma, Lefteris Kampianakis, Alex Hoang, and Andreas Pedross-Engel. Without their guidance and support, this work would not be possible.

DEDICATION

to my parents

Chapter 1

INTRODUCTION

To make the simplest possible wireless sensor device, one would need a sensor, a power source, digital logic, and some means of wireless communication. There is high demand for such a device, as an ultra-low-cost, minimum complexity sensor could be used to measure various quantities (temperature, sound, pressure, humidity, motion and position) for various applications (machine monitoring, process monitoring, asset tracking, safety and surveillance) in a range of industries (automotive, food and beverages, oil and gas, healthcare and pharmaceuticals, manufacturing). A temperature sensor, for example, could be used to keep track of the temperature of machines in an industrial factory, to gather data on the temperature of soil in a large piece of farmland, or to control the air-conditioning in a corporate office building. The ideas presented in this thesis will demonstrate one example of a simple sensor, one that requires nothing more than a battery-powered digital logic device to send sensor data wirelessly. With ZeroScatter, we show that wireless transmission of sensor data can be performed with backscatter from billions of existing commodity microcontrollers (MCUs) and field-programmable gate arrays (FPGAs), with zero added components.

Backscatter communication offers the potential for significant size, cost, and power savings in data uplinks for wireless sensors. These advantages are achieved by re-partitioning the wireless communication link to separate carrier generation from modulation. Backscatter communication can be compared to the flashlight-mirror model depicted in Fig. 1.1. In this model, suppose two people are in a dark room trying to communication with one another. If one person, Alice, has a flashlight and the other, Bob, has a mirror, Bob can effectively send information to Alice by moving the mirror in different orientations to modify and reflect the light from the flashlight. Alice can then observe different reflections depending on

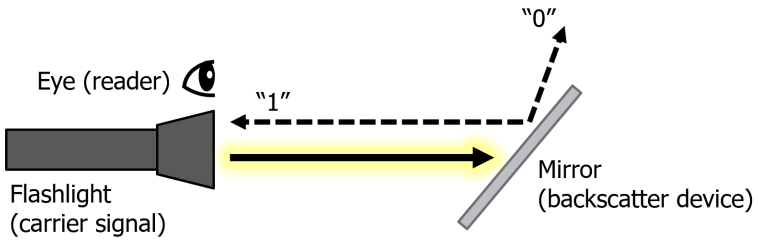

Figure 1.1: Flashlight-mirror analogy for backscatter communication: moving the mirror (backscatter device) in different orientations modifies and reflects the light provided by the flashlight (carrier signal).

how Bob moves the mirror. It is important to emphasize here that Alice and Bob do not need two flashlights to communicate: they only need one active device supplying power (the flashlight) and one passive device that can reflect that power (the mirror). This is precisely how backscatter communication works with RF signals. A backscatter device, like the mirror, modifies and reflects an incoming RF carrier signal, like the light from the flashlight, to send information. In other words, by reflecting the signal or not, the backscatter device can transmit a 1 or a 0. In this work, the RF equivalent of the flashlight is a carrier source, which could be a dedicated continuous wave (CW) source or an ambient signal. The RF equivalent of the mirror is a dipole antenna with a switched impedance. With the ZeroScatter approach, we show that digital I/O pins can perform the switched impedance function.

1.1 Thesis Outline

The remainder of this thesis document is organized as follows. Chapter 2 presents prior work regarding backscatter wireless tags and ambient backscatter communication systems. Chapter 3 describes the development of the BPSK and QPSK ZeroScatter wireless sensor tags. The design and optimization of the 4-dipole antenna array is presented in Chapter 4, and the setup of the direct sampling digital receiver and receiver capture of ZeroScatter data is detailed in Chapter 5. Chapter 6 summarizes the results and presents our conclusions and ideas for future work.

Chapter 2

BACKGROUND

The use of modulated backscatter for communication dates to the 1940s [1]. Today, backscatter communication is widely used by billions of battery-free passive radio frequency identification (RFID) tags implementing amplitude shift keying (ASK) or phase shift keying (PSK) backscatter data links. Recent research in backscatter communication includes the development of higher-order modulation such as quadrature amplitude modulated (QAM) backscatter [2] as well as the development of faster and more power-efficient backscatter modulators [3, 4] and the development of approaches to make backscatter communication compatible with conventional wireless standards such as Bluetooth Low Energy [5, 6] and WiFi [7].

One example of an existing backscatter-based wireless sensor is the Wireless Identification and Sensing Platform, or WISP, developed by Joshua R. Smith and his team at the University of Washington [8]. WISP is a family of sensors that are powered and read by UHF RFID readers. WISPs harvest their power from the RF signal generated by the reader and include a fully programmable microcontroller, as well as arbitrary sensors. The architecture of the WISP tag is typical for existing backscatter-based wireless sensors. Fig. 2.1 presents a breakdown of the components that make up these devices. The primary component is digital logic, provided by a microcontroller or FPGA. External sensors send sensor data to the MCU or FPGA, and using that data, digital logic controls a modulator. The modulation causes the antenna to reflect or absorb an incoming RF signal. In order to perform the modulation function, existing MCU and FPGA-based backscatter wireless sensors rely on external components such as RF FETs, PIN diodes, or varactors. If the carrier wave is sending information content, existing backscatter sensors may also need a demodulator to extract

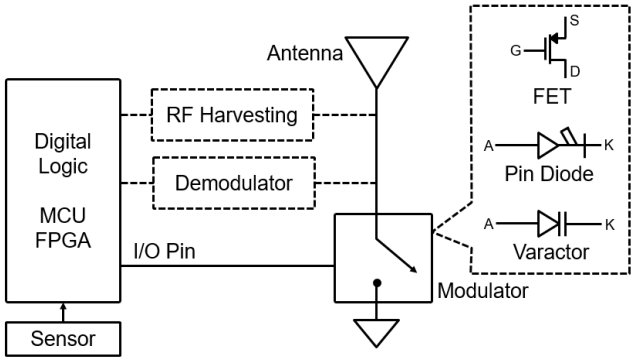

Figure 2.1: Block diagram of a typical backscatter-based wireless sensor. These sensors rely on RF FETs, PIN diodes, and varactors for modulation.

that information. In addition, existing MCU and FPGA-based ambient backscatter wireless sensors may implement energy harvesting circuits to harness the power of the incoming RF carrier signal and transmit data without a battery. Unlike prior MCU-based sensor tags, ZeroScatter does not require any external modulation components to perform backscatter communication. For applications in which a battery would not be practical, the battery on the ZeroScatter tag could be replaced with an RF, vibration, or solar energy harvester.

Early work in ambient backscatter, a passive communication system and method, includes that of Curt Carrender, as shown in his 2005 patent [9]. In such a system, devices configured to receive ambient radiation can communicate, or read and write data, by modulating their reflections of the existing radio frequency (RF) signals. Because backscatter devices do not need to generate radio waves, backscatter communication is orders of magnitude more power-efficient than traditional radio communication, while the use of ambient signals further eliminates the need for a dedicated carrier source [10]. Recent research in ambient backscatter includes the characterization of detection performance in ambient communication systems [11], as well as the performance analysis of wireless broadband networks with ambient backscatter devices [12] and the integration of ambient backscatter techniques in RF-powered cognitive radio networks (CRNs) [13].

An example of an ambient backscatter system using ultra-low-power devices is presented in [10]. The approach, outlined in Fig. 2.2, leverages existing TV transmissions as carrier

signals. Among the strongest ambient signals in the ultra-high frequency (UHF) band, TV broadcast signals can transmit up to 1 MW effective radiated power (ERP). These signals can reach 100 mi from the tower in flat terrain and up to 45 mi in denser terrain, making them a good candidate for wide-area wireless communication in urban environments [10]. In the setup in Fig. 2.2, Alice reflects or absorbs the incoming ambient signal from the TV tower to backscatter data. These signals can can be decoded by other ambient backscatter devices, like Bob. To legacy receivers, this signal is an additional source of multi-path, and the original transmission must be decoded. The design relies on wideband receivers for TV and cellular applications to compensate for multi-path wireless channels and account for the additional backscattered data path.

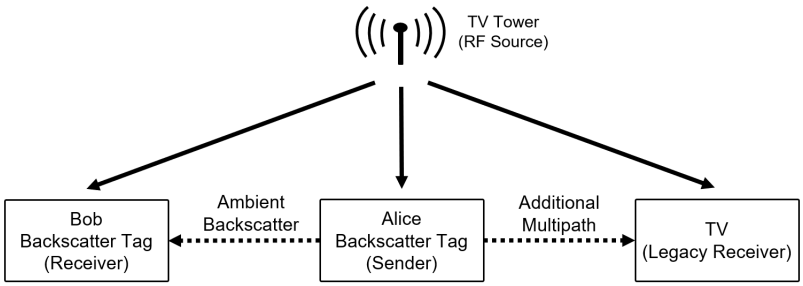

Figure 2.2: Ambient backscatter communication between two passive, battery-free devices and resultant multi-path.

In our ambient ZeroScatter system, we also use digital television (DTV) signals in the 500-600 MHz range to backscatter wireless sensor data from the ZeroScatter tag, as DTV signals are strong and present in urban environments. However, our tag does not require any external components to perform modulation, and our design does not rely on legacy receivers to decode the transmission. Instead, it leverages the individual dipole elements from a 4-dipole antenna array developed for a passive radar application. The dipole antennas capture ambient DTV signals and the direct sampling digital receiver processes the backscattered information. Future work with the existing 4-dipole antenna array could include localization of the ZeroScatter tag.

Chapter 3

BPSK AND QPSK ZEROSCATTER TAGS

This chapter is based in part on work published and presented at the 2019 IEEE Wireless Sensors and Sensor Networks Conference in Orlando, Florida [14].

This chapter presents ZeroScatter, a novel low-cost and low-complexity approach for backscatter communication. ZeroScatter uses existing digital I/O pins to serve double-duty as backcatter modulators. Using the ZeroScatter approach, backscatter communication can be supported by billions of existing microcontrollers (MCUs, such as the PIC, AVR, ARM, etc.) and field-programmable gate arrays (FPGAs). Unlike prior MCU-based sensor tags [15], zero external components are needed to perform binary phase-shift keying (BPSK) backscatter. We also demonstrate the ZeroScatter approach for quadrature phase-shift keying (QPSK) backscatter modulation, implemented with a combination of two digital I/O pins and the addition of two external capacitors. Our demonstration BPSK ZeroScatter tag uses the PIC12LF1552 MCU as shown in the photo of Fig. 3.1 and schematic of Fig. 3.2.

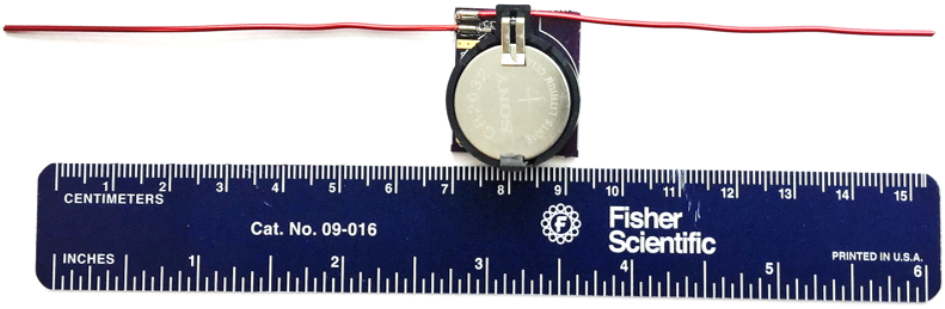

Figure 3.1: Photo of the ZeroScatter prototype.

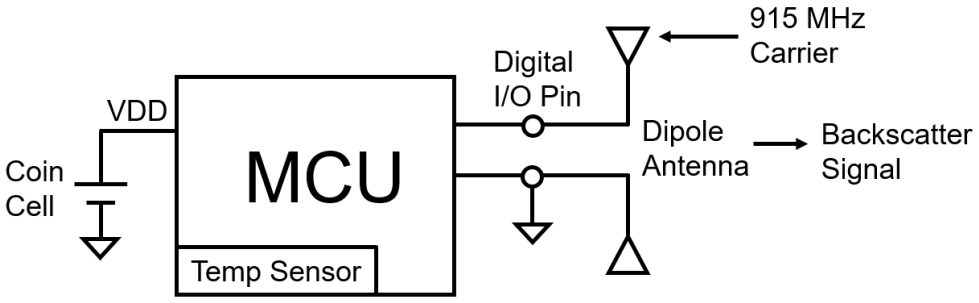

Figure 3.2: Schematic of the ZeroScatter prototype.

3.1 Digital I/O Pins as Backscatter Modulators

As shown in Fig. 3.3(a), a typical on-chip digital I/O pin structure consists of a tri-state output driver combined with an input buffer. The key concept behind ZeroScatter is that digital pins with a selectable direction (input vs. output) present two different RF impedances with respect to ground, depending on the pin direction. From a digital perspective, input mode must have a high impedance to avoid loading the circuit that's driving the pin, and output mode must have a low impedance to enable fan-out.

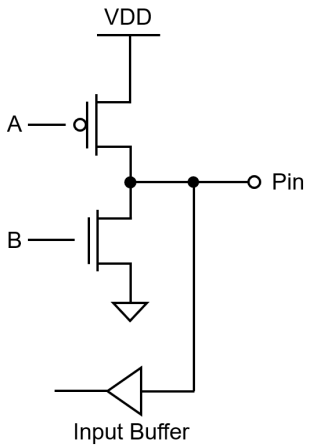

(a)

	A	B	Pin State
Output mode	1	1	Output Low
Output mode	0	1	Invalid - Shorted VDD-GND
Output mode	0	0	Output High
Input mode	1	0	Tri-state Pin Floating

(b)

Figure 3.3: (a) Typical I/O pin structure and (b) pin state diagram.

Surprisingly, this behavior extends to UHF and microwave frequencies well beyond the specified toggle frequency for the pin. While parasitics at the I/O pins prevent them from behaving as ideal RF open and short circuits, digital I/Os present two distinct RF impedances, and this is sufficient to enable backscatter communication when the pin is directly connected to an antenna, without any impedance matching components. Pin direction is determined by logic that implements the behavior shown in Fig. 3.3(b).

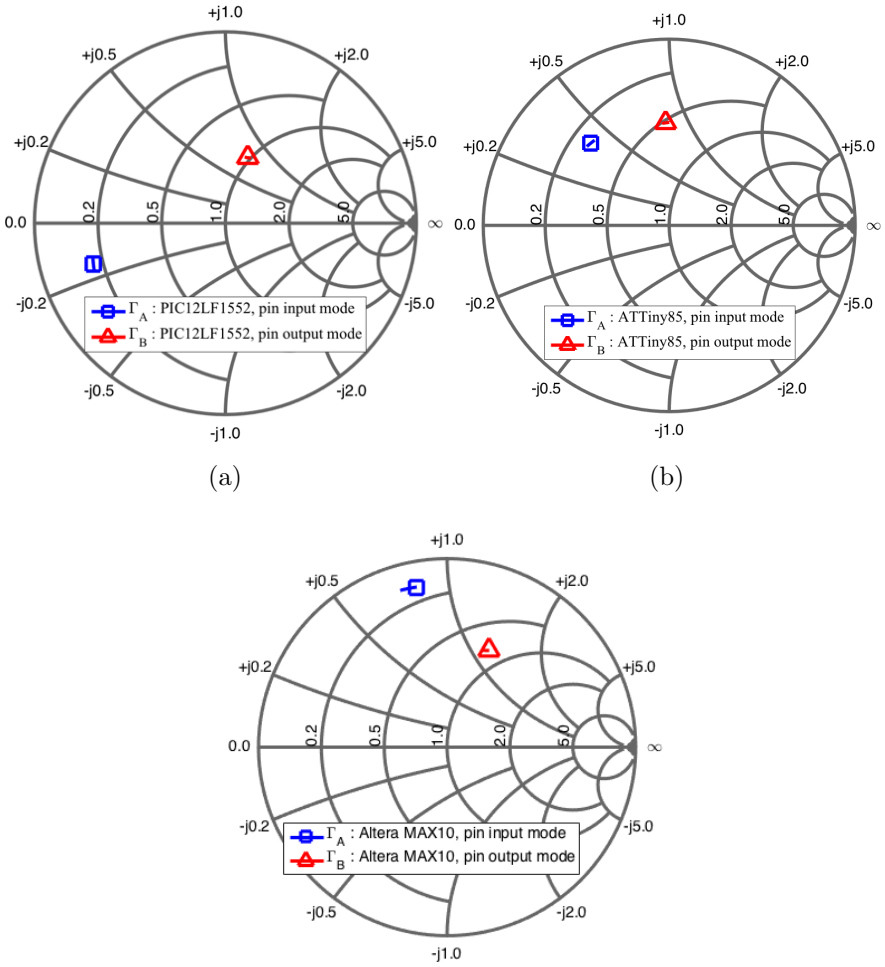

Figure 3.4: Smith charts of measured I/O pin impedances in input and output modes over the 902-928 MHz band: (a) Microchip PIC12LF1552 MCU, (b) Atmel ATTINY85 MCU, (c) Altera MAX10 10M08SCE144C8G FPGA.

The Smith charts of Fig. 3.4 show the measured RF pin impedances of the PIC12LF1552 and ATTINY85 MCUs, and the Altera MAX10 FPGA. These measurements were de-embedded to the package pin, and were taken at an RF power level of 0 dBm. At 915 MHz, the measured $\Delta\Gamma$ between the two BPSK symbol states Γ_A and Γ_B are $0.8092 + j0.5565$ (PIC12LF1552), $0.4041 + j0.1099$ (ATTINY85), and $0.3843 - j0.3365$ (MAX10).

3.2 BPSK ZeroScatter Prototype Sensor Tag

The prototype BPSK ZeroScatter sensor tag consists of only two components: a PIC12LF1552 MCU, and a 3V lithium coin cell. A 16 cm wire dipole, resonant at 915 MHz, forms the antenna. The MCU is programmed to toggle between input and output directions of the pin's tri-state register, thus backscattering a BPSK data stream at a bit rate of 9.4 kbps. The most-significant byte of the PIC's on-chip temperature sensor forms the sensor data payload. A flow chart of the ZeroScatter prototype sensor code is shown in Fig. 3.5. The 4-byte packet described in Table 3.1 is sent least-significant bit first.

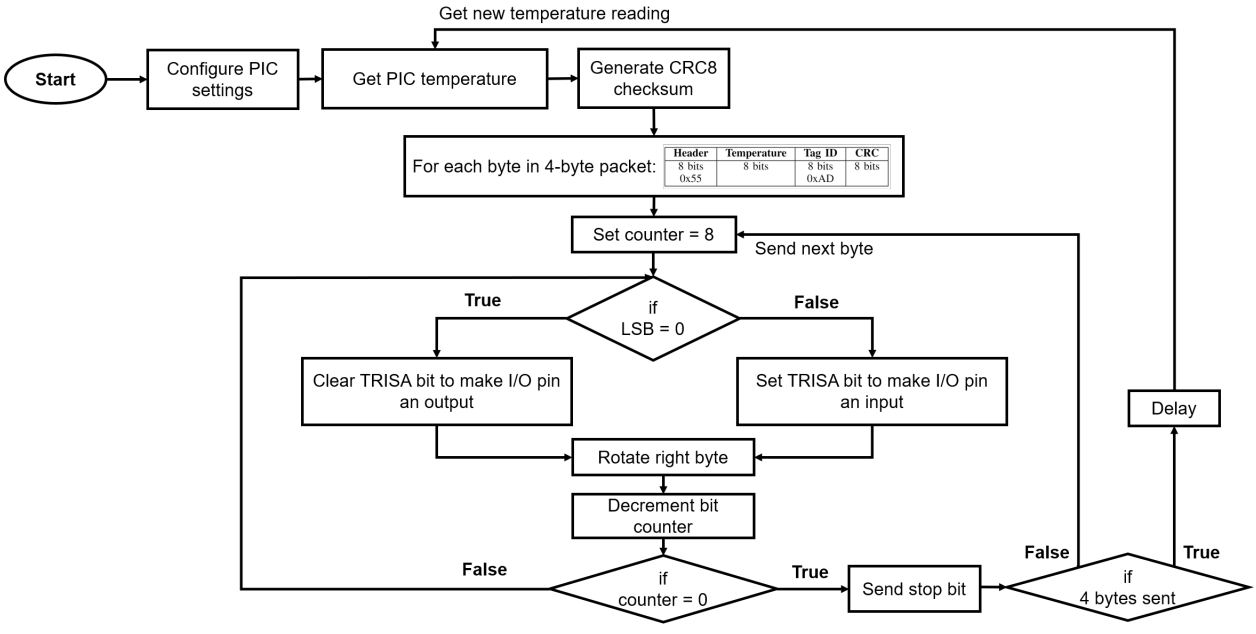

Figure 3.5: ZeroScatter wireless sensor code flow chart.

Table 3.1: ZeroScatter 32-bit packet data format

Header	**Temperature**	**Tag ID**	**CRC**
8 bits	8 bits	8 bits	8 bits
0x55		0xAD	

3.2.1 Experimental setup

As shown in the block diagram of Fig. 3.6(a) and photos of Fig. 3.6(b, c), the test setup consists of an Agilent signal generator providing an unmodulated +10 dBm, 915 MHz carrier, which is split into two paths. The TX path drives an L-Com HG72710LP log-periodic Yagi antenna with a specified gain of 10 dBi. The RX path uses the same carrier source

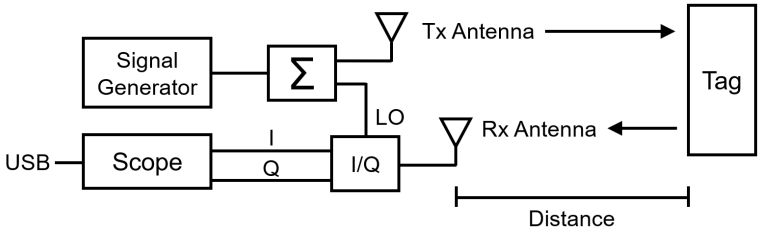

(a)

(b)

(c)

Figure 3.6: (a) Block diagram of the experimental setup. (b) Photo from the perspective of the equipment cart and (c) Photo from the perspective of the ZeroScatter tag.

to provide a homodyne local oscillator (LO) signal to a Linear Technology LTC5575 I/Q demodulator with a specified conversion gain of 3 dB and a noise figure of 12.8 dB. The I/Q demodulator was fed from a bistatic receiving antenna, also an HG72710LP. An Agilent MSO-X oscilloscope records the I/Q baseband signals for post-processing in MATLAB.

3.2.2 Backscatter signal strength validation

To verify that the MCU pin is indeed producing usable backscatter, an Agilent spectrum analyzer (SA) was first connected to the receiving antenna, the MCU was temporarily programmed to send a continuous header of 0x55 (0101 0101 binary), and the observed backscatter subcarrier power was recorded from the SA. Backscatter signal strength was measured at distances ranging from 0.3 m to 3.5 m in increments of 0.2 m. The resulting measured signal strength is presented in Fig. 3.7 along with the predicted value from a free-space backscatter link budget ($1/d^4$) using the previously described parameters. We attribute the model-vs-measurement discrepancy to multipath in the hallway.

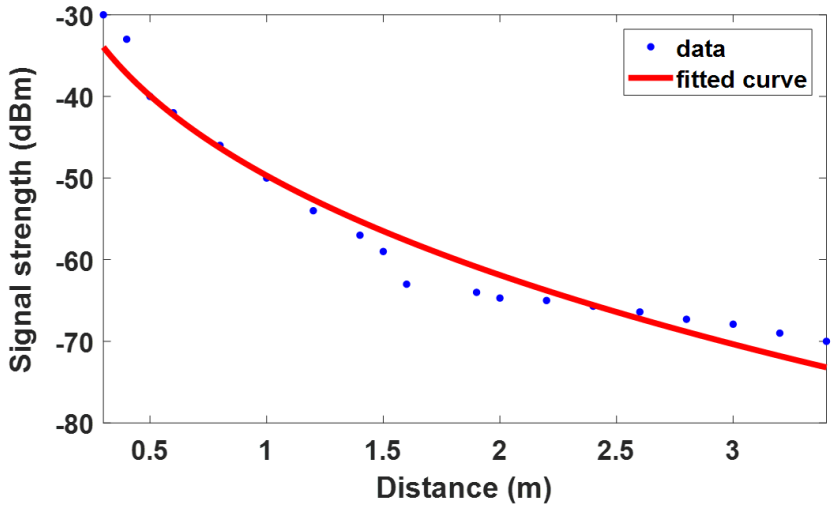

Figure 3.7: Measured backscatter signal strength as a function of tag distance, plotted with the theoretical $1/d^4$ free-space backscatter link budget.

3.2.3 Over-the-air (OTA) data transfer validation

After measuring the received signal strength, the MCU was reprogrammed to send the packet data structure shown in Table 3.1. After the captured I/Q baseband is filtered and phase rotated onto the real axis, the bitstream is recovered. Fig. 3.8(a, b) shows examples of the BPSK data stream as captured at distances of 1 m and 3 m, respectively. A signal-to-noise power ratio exceeding 20 dB and no bit errors are observed in both examples.

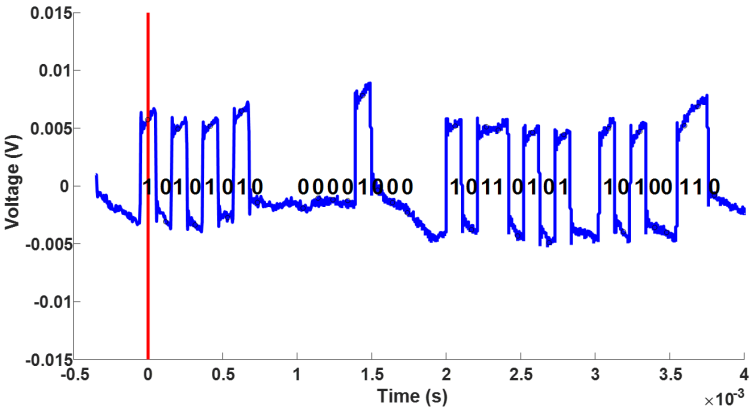

(a)

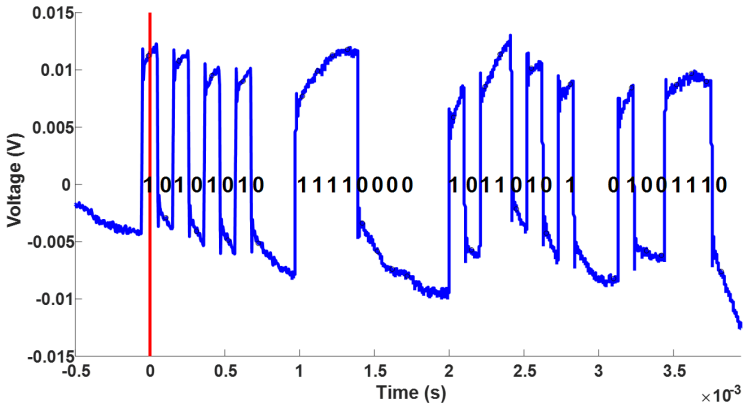

(b)

Figure 3.8: Measured waveform of baseband data at a distance of (a) 1 m from the tag and (b) 3 m from the tag. The red line indicates the detected start-of-header.

3.3 QPSK Backscatter with Two Digital I/O Pins

In order to achieve higher data rates at the same symbol rate, we have conducted preliminary work using multiple digital I/O pins in concert to generate multiple symbol states for M-ary modulation. For example, by using two digital I/O pins in parallel, four impedance states, and thus four distinct backscattered symbols (M = 4 PSK), can be realized. Since adjacent digital I/O pins are expected to have similar impedances in the input and output state, we considered adding series and/or shunt impedances between the pins to separate the symbol states impedances as far as possible on the Smith chart. Such series or shunt elements can take the form of either transmission line elements or lumped element components.

3.3.1 M = 4 PSK (QPSK) ZeroScatter Tag Modeling and Measurement

To determine the feasibility of implementing M = 4 PSK (QPSK) backscatter modulation with two I/O pins, we connected two I/O pins (RA4 and RA5) on the PIC12LF1552 MCU directly to an SMA connector. The tag was programmed to set the pins into each of the four PSK symbol states S_0 through S_3 as shown in Table 3.2.

Table 3.2: QPSK ZeroScatter Symbol States

Symbol	**PIN A (RA4)**	**PIN B (RA5)**
S_0	Input	Input
S_1	Input	Output
S_2	Output	Input
S_3	Output	Output

An initial vector network analyzer (VNA) measurement verified that the setup presented four RF impedances with respect to ground, depending on the pin directions. However, symbols S_1 and S_2 proved to be relatively close in impedance, which is not unexpected due to our use of two adjacent digital I/O pins on the MCU. To separate these symbol states as far

apart in impedance as possible, we added two external lumped impedances (capacitors) in a series/shunt combination. We first simulated this configuration for a simplified circuit model using AWR Microwave Office as shown in Fig. 3.9. A schematic diagram of the resulting QPSK ZeroScatter tag is displayed in Fig. 3.10.

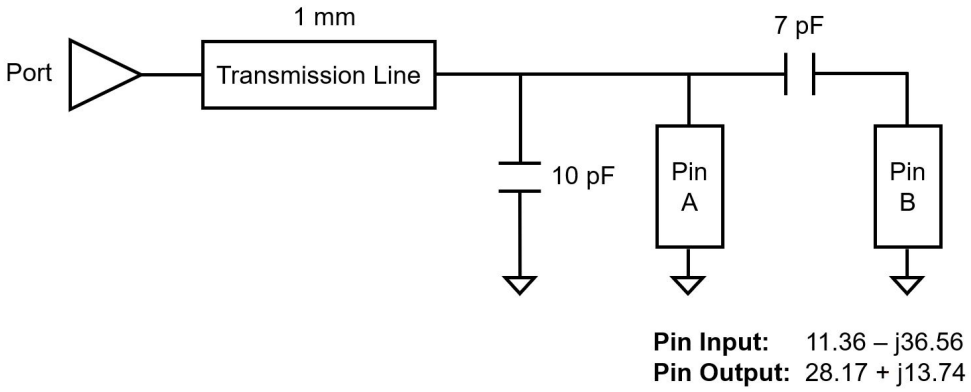

Figure 3.9: AWR Microwave Office simulation setup.

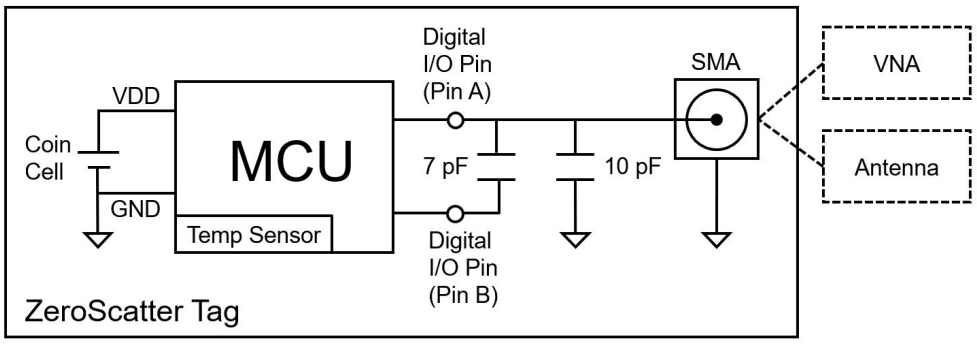

Figure 3.10: Schematic of implemented QPSK ZeroScatter tag.

We found fair agreement between the AWR simulation results and the physical measurement with the VNA, as shown in Fig. 3.11. Compared to the simulation results, the measurement showed a slight clockwise rotation about the center of the constellation which we attribute to small measurement errors when de-embedding the MCU pin impedances.

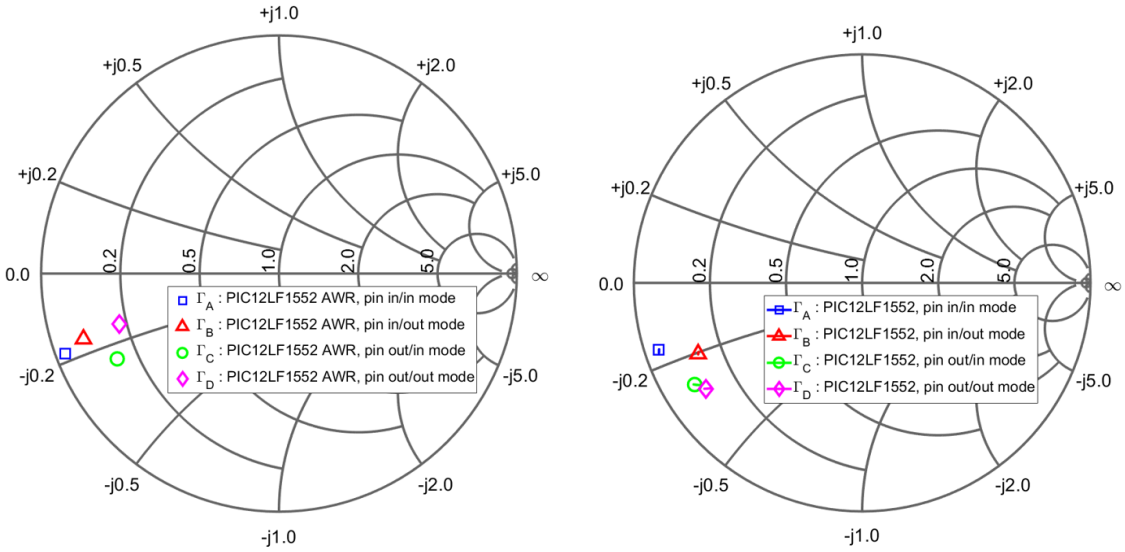

(a) (b)

Figure 3.11: Smith charts of (a) simulated and (b) measured I/O pin impedances on the PIC12LF1552 microcontroller for four symbol states S_0 through S_3 over the 902-928 MHz band.

As can be seen in Fig. 3.11, the four symbol states are not perfectly symmetric about a common centroid on the Smith chart. The consequence of this non-ideal symbol placement is a reduction in the minimum distance between symbols compared to the ideal QPSK constellation. This will in turn result in worse bit error rate (BER) than could otherwise be achieved. We expect that a more careful choice of external series/shunt impedances will improve the symmetry of the constellation.

3.3.2 Connectorized and over-the-air (OTA) validation of the QPSK ZeroScatter tag

The QPSK ZeroScatter tag was characterized in both connectorized and over-the-air (OTA) test setups. The PIC MCU was programmed to continuously switch among symbol states S_0 through S_3, thus backscattering a QPSK data stream at a symbol rate of 18 ksymbols/s, yielding a bit rate of 36 kbps. An Ettus Research Universal Software Radio Peripheral (USRP) B210 and a custom self-jammer cancellation circuit were used to generate a 915 MHz

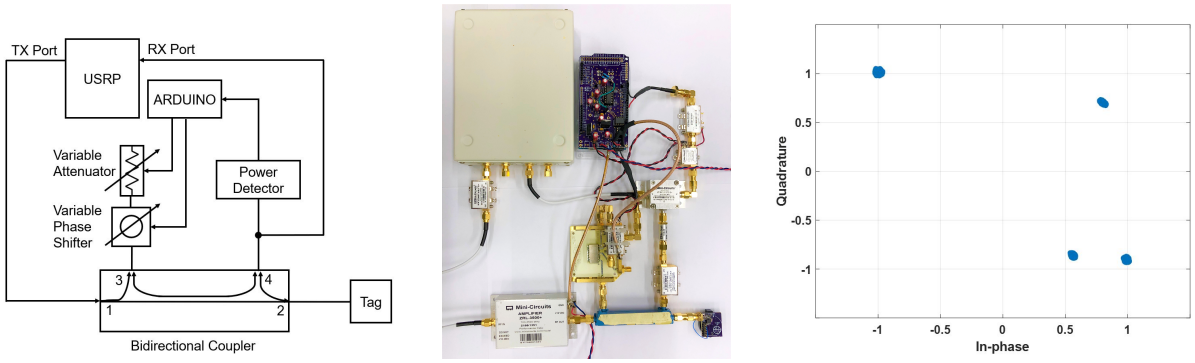

(a) (b) (c)

Figure 3.12: Connectorized test setup: (a) Block diagram (b) Photo (c) Measured constellation.

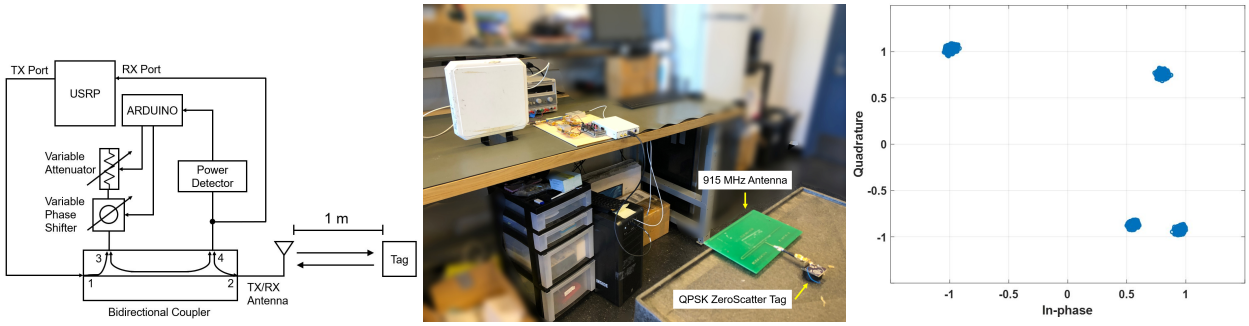

(a) (b) (c)

Figure 3.13: Over-the-air test setup: (a) Block diagram (b) Photo (c) Measured constellation.

carrier and demodulate the backscattered QPSK signal. The self-jammer cancellation circuit, described in detail in [16], is used to suppress the unwanted feedback of the transmitted carrier into the USRP receiver port. As shown in the block diagram of Fig. 3.12(a) and photo of Fig. 3.12(b), the connectorized test setup consisted of a self-jammer cancellation circuit and USRP connected directly to the QPSK ZeroScatter tag. The USRP connects to a PC for signal processing using the GNURadio framework.

In the over-the-air test setup, shown in Fig. 3.13, a commercial 8 dBi right hand circularly polarized (RHCP) antenna is instead connected to the USRP via the self-jammer cancellation

circuit. The QPSK ZeroScatter tag is connected to a 4 dBi printed circuit Yagi antenna placed at a distance of 1 m from the USRP antenna. Fig. 3.12(c) shows the measured symbol constellation for the connectorized test setup, while Fig. 3.13(b) shows the measured symbol constellation for the over-the-air test setup. The measured constellations show good agreement with both the simulated and measured VNA results.

Chapter 4

500-600 MHZ DIPOLE ANTENNA ARRAY FOR THE DIGITAL TELEVISION BAND

The ZeroScatter concept was originally prototyped with a dedicated continuous wave (CW) carrier supplied by an RF signal generator in the 915 MHz band. However, the infrastructure to provide a carrier may not always be present in every environment, especially in wide-area outdoor applications. An alternative approach is to leverage an existing carrier source already present in the environment. Among the strongest such ambient signals are digital television (DTV) signals in the UHF band. DTV signals have been previously exploited as an illumination source for passive radar [17, 18]. The 4-element array presented in this section could be used for passive radar, or alternatively as an illumination source and/or receiver for backscatter-based wireless sensor tags such as the ZeroScatter tag. The full antenna array described here is not needed for the ZeroScatter experiments detailed in Chapter 5, but the individual dipole elements were used in the final system as transmitting and receiving antennas.

The array itself was originally designed in conjunction with our collaborators at the University of Washington Applied Physics Laboratory (APL) for a directional signal processing application for radar systems. Although the complete array is not implemented in this specific thesis work, it would be useful for future direction of arrival processing in the ambient ZeroScatter system. The core design objectives for the antenna array were that the antennas were well matched to the 50 Ω port across the widest bandwidth possible in the DTV band and that the antennas had the lowest mutual coupling possible given the size constraint from our collaborators at APL.

4.1 Initial Antenna Array Design and Testing

The initial antenna array, designed by our collaborators to capture DTV signals for a passive radar application, consisted of four half-wave dipoles, each 26 cm long and oriented at a 45° angle. The dipoles were mounted to a copper "throwing star" shaped ground plane providing mechanical support. The dipoles and ground plane were mounted 12 inches above a metal electronics box containing the receiver hardware using non-conductive supports.

4.1.1 Simulation and measurement of Configuration A: Throwing Star

Fig. 4.1(a) shows the initial antenna array, which will be referred to as Configuration A: Throwing Star, that was simulated in the Computer Simulation Technology (CST) Microwave Studio design environment. The base electronics box, copper throwing star, and four dipole antennas oriented at 45° are all visible. Fig. 4.1(b) presents a photo of the setup. The dipole antennas themselves, show in Fig. 4.2 consisted of two copper wires, each 13 cm in length, with one connected to the center pin of an SMA connector and one connected to ground.

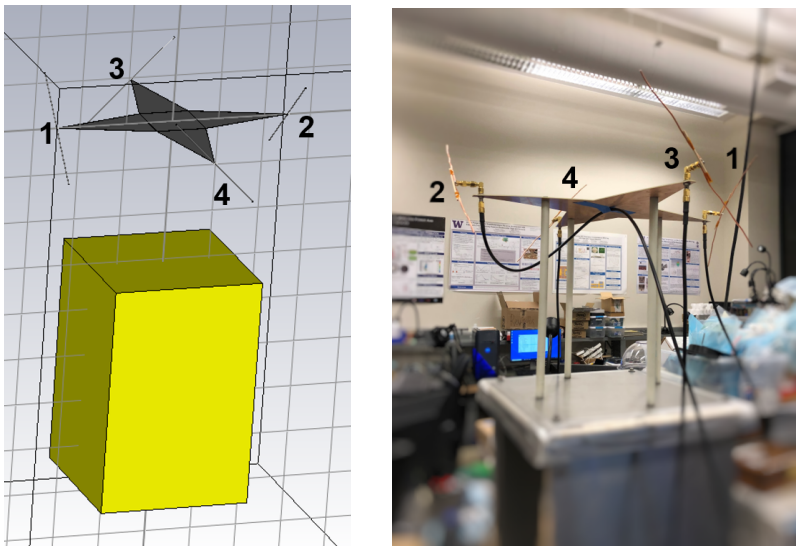

(a) (b)

Figure 4.1: Initial antenna design and setup in (a) CST and (b) lab environment.

Figure 4.2: Initial antenna design, consisting of two copper wires (13 cm each), one connected to the center pin of an SMA connector and one connected to ground.

In the CST design environment, we simulated the return loss of port 1 (S11) and the mutual coupling between port 1 and ports 2, 3, and 4 (S21, S31, S41). For the lab setup, we used a vector network analyzer (VNA) to measure the 4-port S-parameters. In our setup, the VNA measured 2 ports simultaneously, allowing us to measure S11, representing the return loss or matching of the antenna, and S21, the mutual coupling between a pair of antennas. We measured the return loss of port 1 (S11) and mutual coupling between port 1 and ports 2, 3, and 4 (S21, S31, S41). The results from simulation and experimental measurements were qualitatively very similar, allowing us to optimize the antenna design in simulation without having to manufacture several test designs. For the initial experimental antenna setup, we had a return loss of approximately 25 dB with a resonance frequency of 535 MHz. The mutual coupling was worst around 200 MHz and 400 MHz (approximately −10 dB) and between −20 dB and −30 dB around the resonance.

4.1.2 Simulation of metal electronics box at various positions

One aspect of the design we were able to explore in simulation was the position of the metal electronics box with respect to the antenna array. As the box is made of aluminum, we would expect that it would have an effect on the radiation pattern of the antenna array. We monitored both the far-field realized gain and the S-parameters in simulation. As shown in Fig 4.3, the electronics box interferes with one of the main lobes of the antenna pattern. As we move the electronics box farther away, the pattern becomes less deformed. In Fig 4.4, we show S-parameters for the three cases. As we move the electronics box farther away, the mutual coupling around the resonant frequency stays fairly constant.

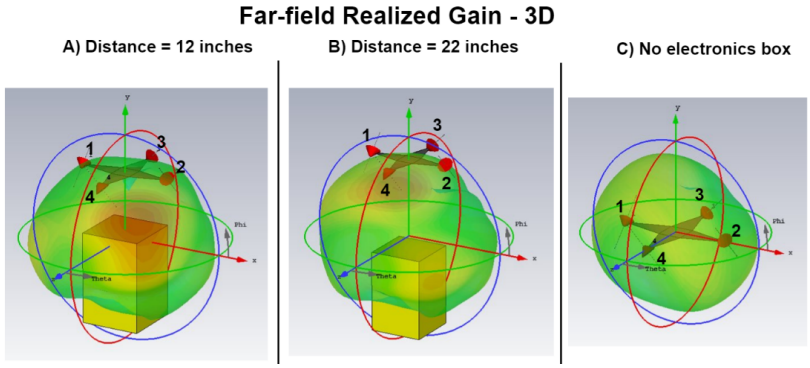

(a)

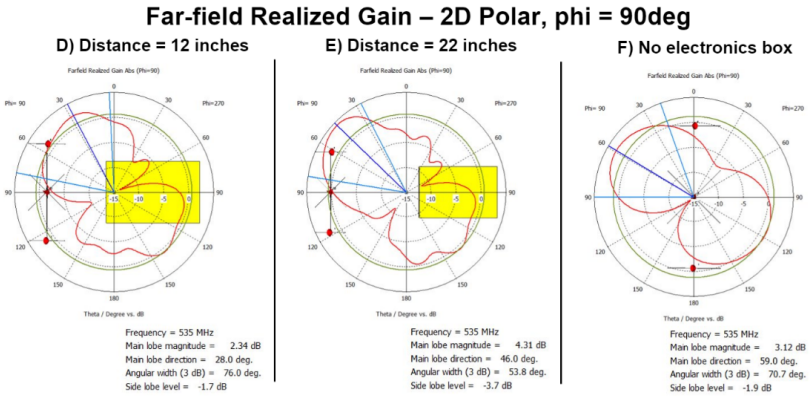

(b)

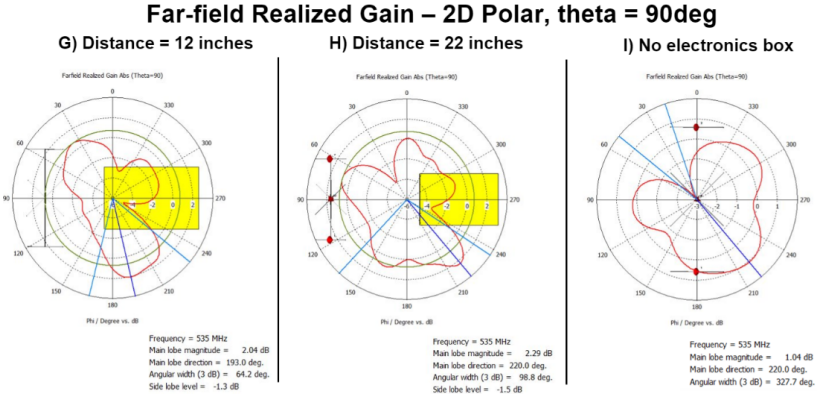

(c)

Figure 4.3: (a) 3D far-field realized gain, (b) Polar far-field realized gain with phi = 90°, (c) Polar far-field realized gain with theta = 90° for an electronics box distance of 12 in (A), 22 in (B), and no electronics box (C), respectively.

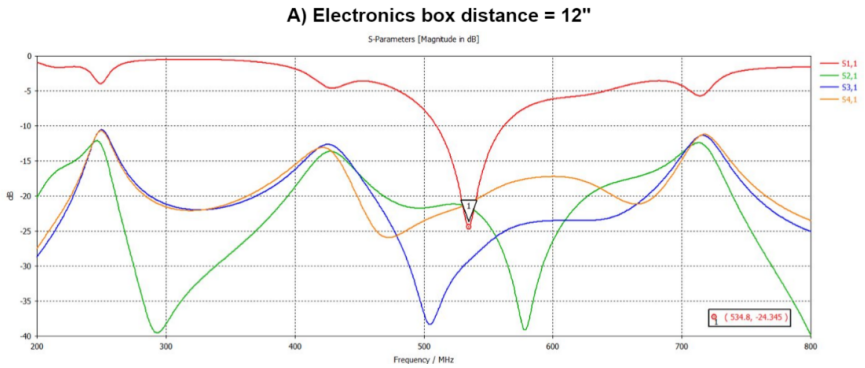

(a)

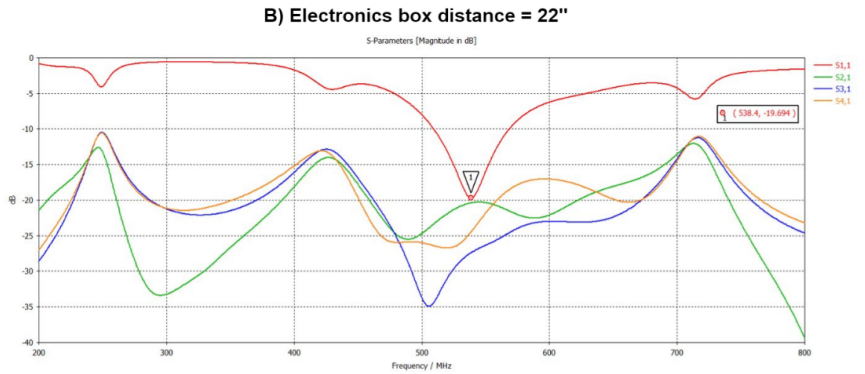

(b)

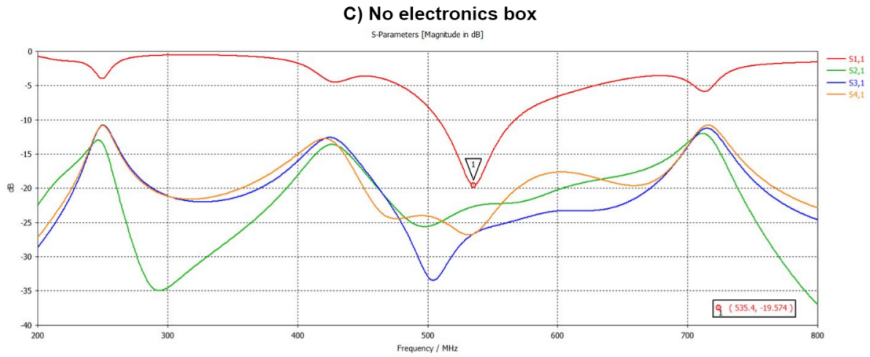

(c)

Figure 4.4: S-parameters for (a) electronics box 12 in. from antenna frame, (b) electronics box 22 in. from antenna frame, and (c) no electronics box.

4.2 Optimization of Antenna Array and Mounting Designs

4.2.1 Vertical dipoles

To improve performance, we simulated several different antenna and mechanical mounting designs. First, we tried orienting the dipoles vertically instead of at 45° angles. Fig 4.5 shows results from these simulations. We found that this change in orientation lessened the effect of the electronics box on the beam pattern, in particular the main beam lobe. This is due to the reduction of current induced in the electronics box. If the dipole elements were horizontally oriented, parallel to the electronics box, there would be maximum coupling between the dipoles and the box. At a 45° angle, the dipole elements are in effect more parallel to the electronics box than if they were vertically oriented. Thus, the dipoles in

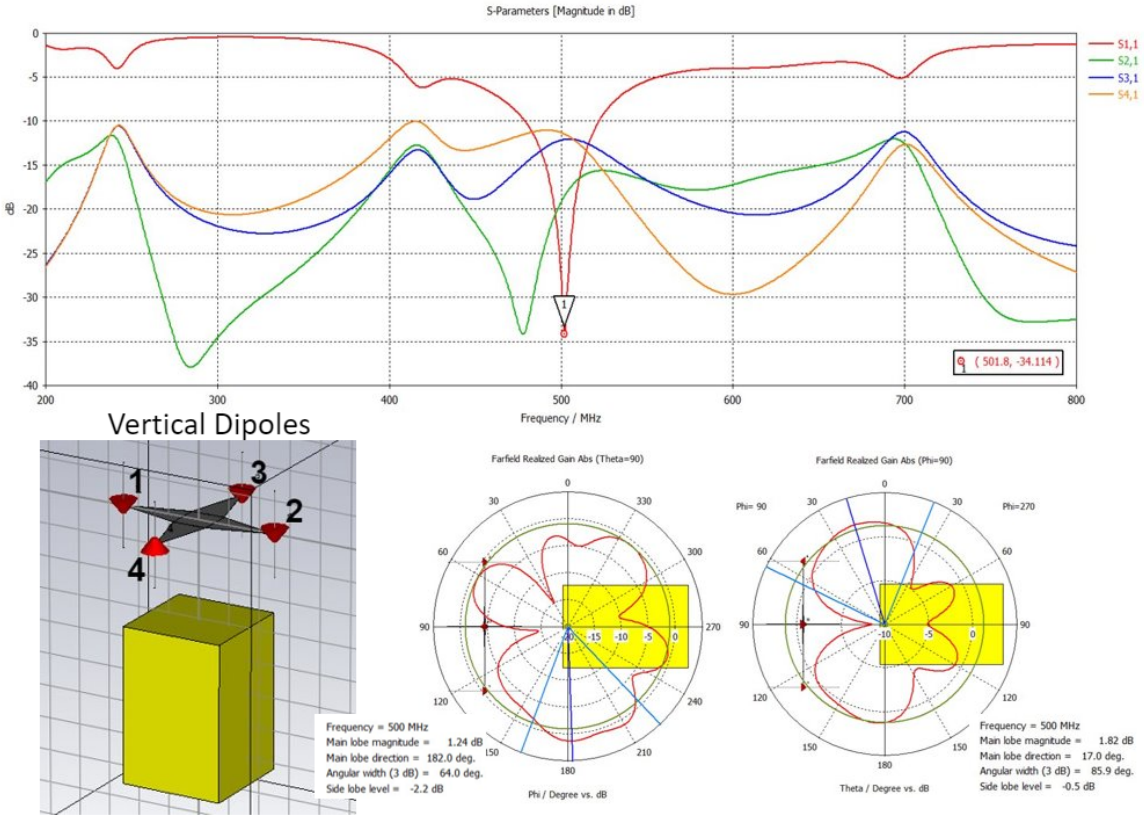

Figure 4.5: Results from orienting dipoles vertically.

the tilted orientation couple more and induce more current in the electronics box, which re-radiates and interferes with the overall beam pattern. The vertical orientation lessens this effect.

4.2.2 Thin tube cross-pattern antenna frame

In addition, we found that removing the conductive copper throwing star and replacing the mounting hardware with an alternative frame having reduced metal surface area improved the beam pattern. Fig 4.6 shows results from this simulation, where we have replaced the throwing star with narrow fiberglass tubes in a cross pattern, making the beam pattern more regular. In this case, the electric field created by the dipoles induced a current in

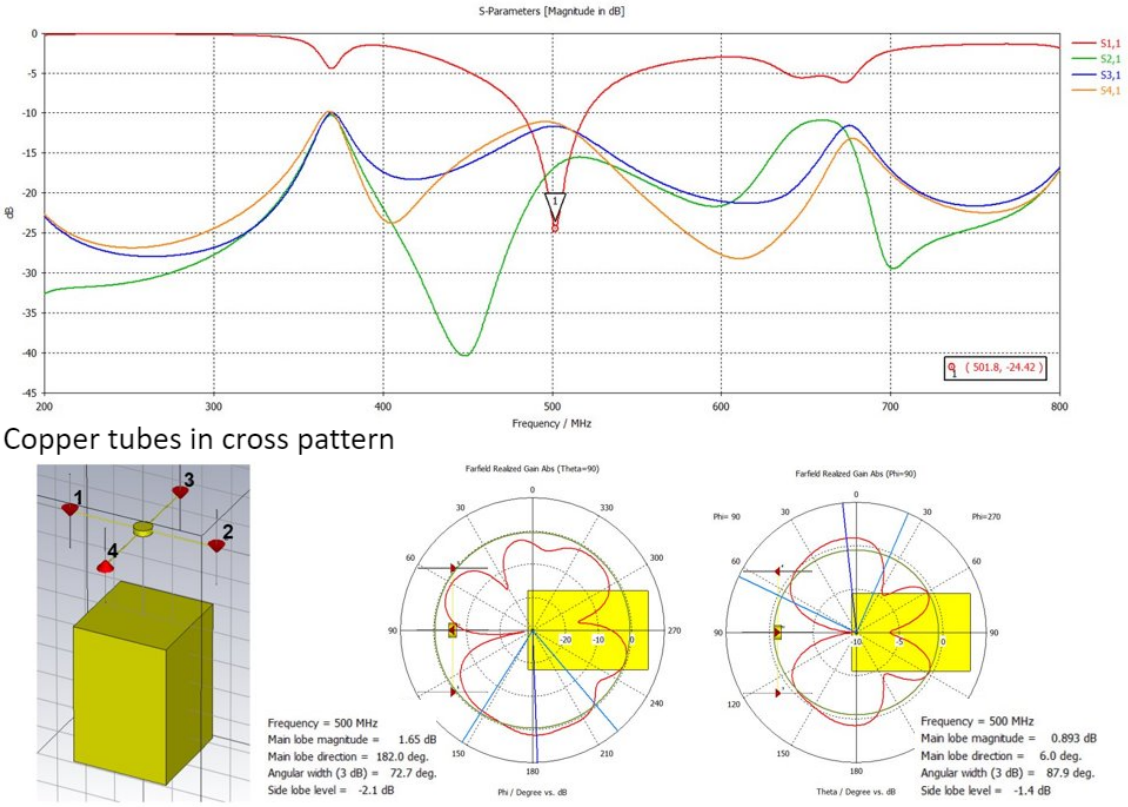

Figure 4.6: Results from replacing throwing star with thin fiberglass tubes.

the throwing star frame. This current in turn created another electric field which interfered with the desired radiation pattern. A thin fiberglass frame, with a lower dielectric loss, thus lessened the interference with the beam pattern.

4.2.3 Balun

In the previous simulations, one side of the dipole was electrically connected to ground and the conductive parts of the mechanical frame (either the throwing star or the tube frame). In our final simulation, we looked at the effect of inserting a balun that would isolate the dipole completely from any conductive material in the frame. As depicted in the simulation results in Fig 4.7, it can be seen the balun improved the beam pattern.

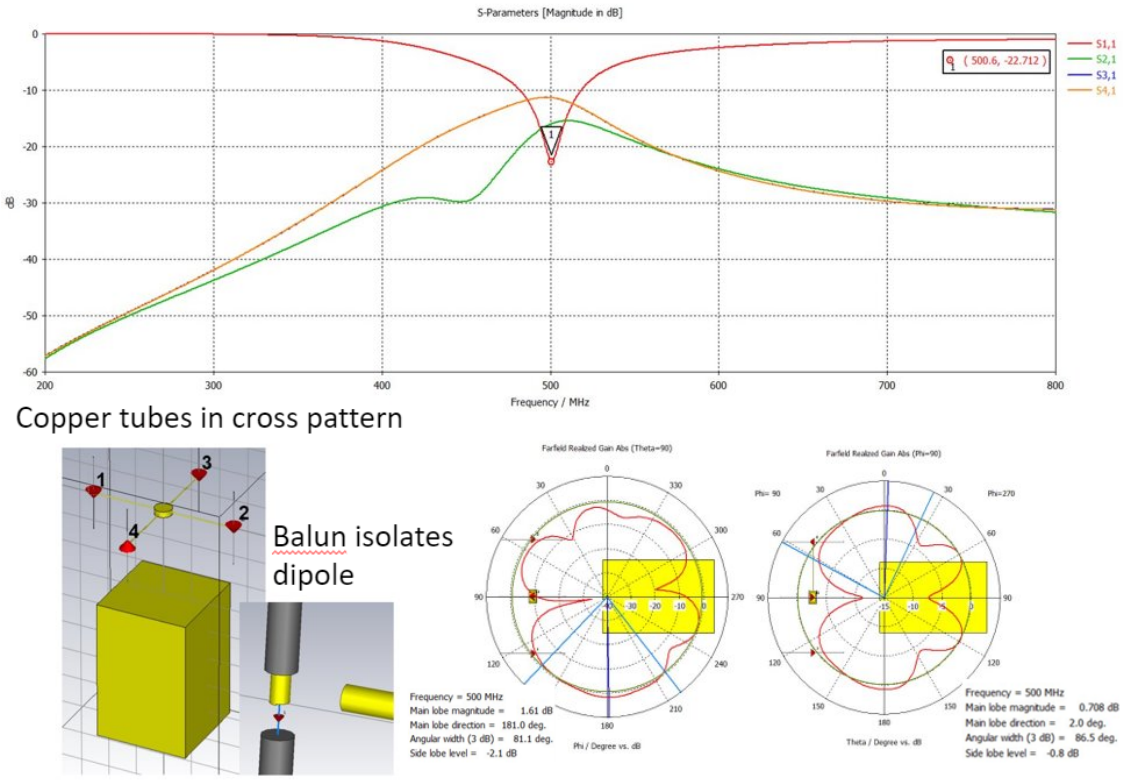

Figure 4.7: Results from adding a balun to the design, which isolates the dipole antenna from conductive components of the frame.

The balun couples a balanced system (dipole antenna) to an unbalanced system (coaxial cable), and it matches the characteristic impedance of the coaxial cable to the antenna's input impedance of 50 Ω. Specifically, it converts the unbalanced coaxial line to a balanced line in order to feed the dipole antenna with discrete patches of forward and backward current. The coupled inductances in the balun prevent current from flowing on the outer shield of the coaxial cable and contain the current to only the inside of the cable. This prevents any radiation from the outer surface that could interfere with the beam pattern. For the physical implementation, we designed and fabricated a printed circuit board (PCB) antenna element made up of a dipole antenna and a Pulse Electronics CX2156NL RF transformer balun. Fig 4.8 shows the PCB fabricated element.

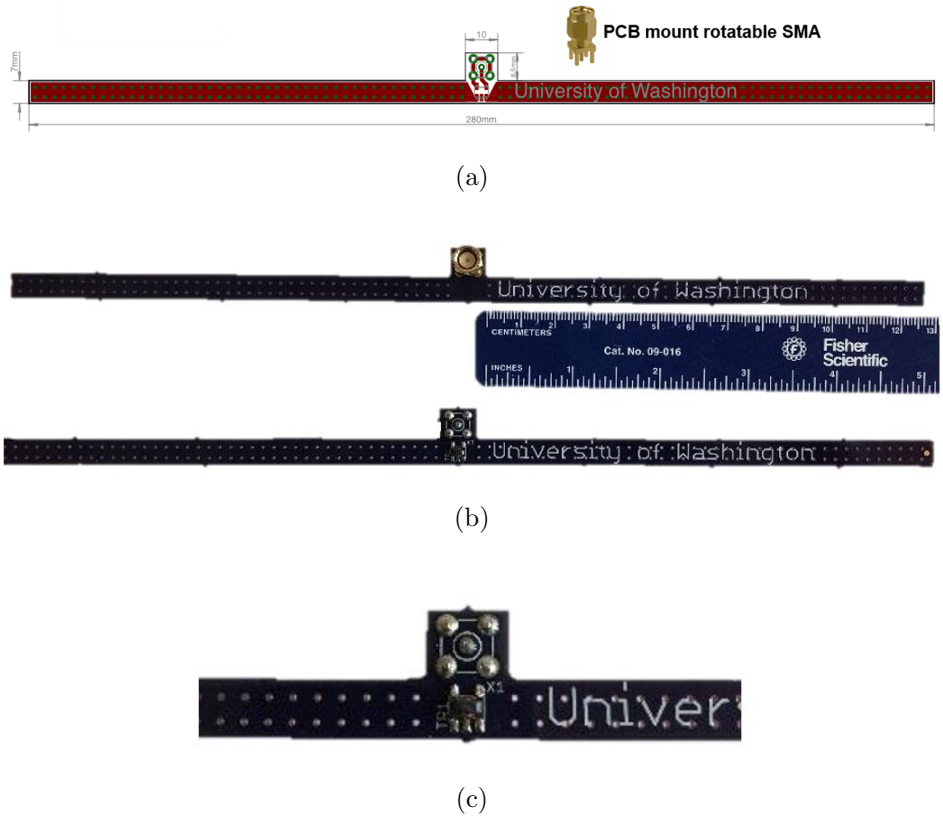

Figure 4.8: (a) Schematic of PCB layout (b) Fabricated PCB antenna with balun (c) Close-up of balun.

4.2.4 Center-to-dipole antenna spacing

Our next optimization step was to explore the antenna spacing in the array. We did this by varying the center-to-dipole spacing in our simulations and observing the S-parameters to monitor mutual coupling and return loss. Fig 4.9 shows a CST capture of the parameter we are changing. We look at equal antenna spacing from the center ranging from d = 15 cm to d = 30 cm in 1 cm steps.

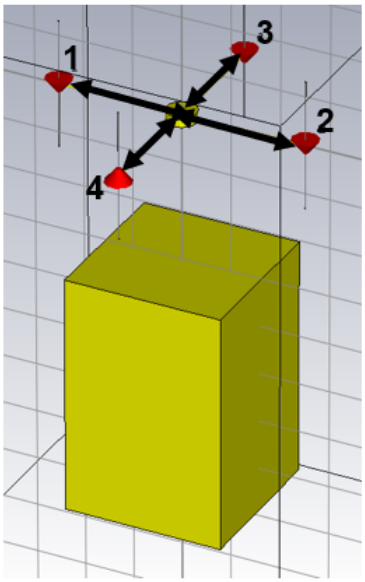

Figure 4.9: Computer Simulation Technology (CST) capture of parameter varied for the antenna center-to-dipole spacing optimization.

Looking at the return loss for antenna 1 (i.e. S11) in Fig 4.10, we note a multi-modal response as we increase the distance. As we sweep the distance from d = 15 cm to d = 20 cm the return loss worsens from approximately 16 dB to about 10 dB, we then see S11 improve from d = 21 cm to d = 27 cm, and finally it again gets worse as we move from d = 28 cm to d = 30 cm. From solely a return loss perspective, d = 27 cm seems to be the best with S11 = -24 dB at the resonance.

Next, we analyzed mutual coupling between nearest neighbors (i.e. S31 and S41) and opposite antennas (S41). Observing the mutual coupling between the nearest neighbor pairs

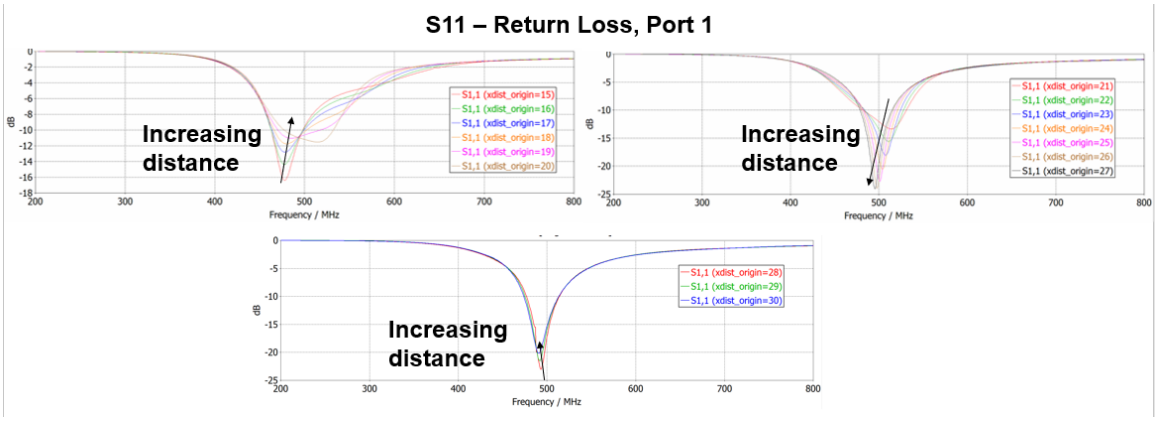

Figure 4.10: Return loss (S11) of varying dipole-to-center spacing in simulation.

to be nearly identical, we only look at S31. Results are shown in Fig 4.11. We note here that we also see a multi-modal response, with increasingly worse mutual coupling from d = 15 cm to d = 24 cm and improved mutual coupling from d = 25 cm to d = 30 cm. However, we can see that S31 does not vary drastically while changing the dipole-to-center distance and

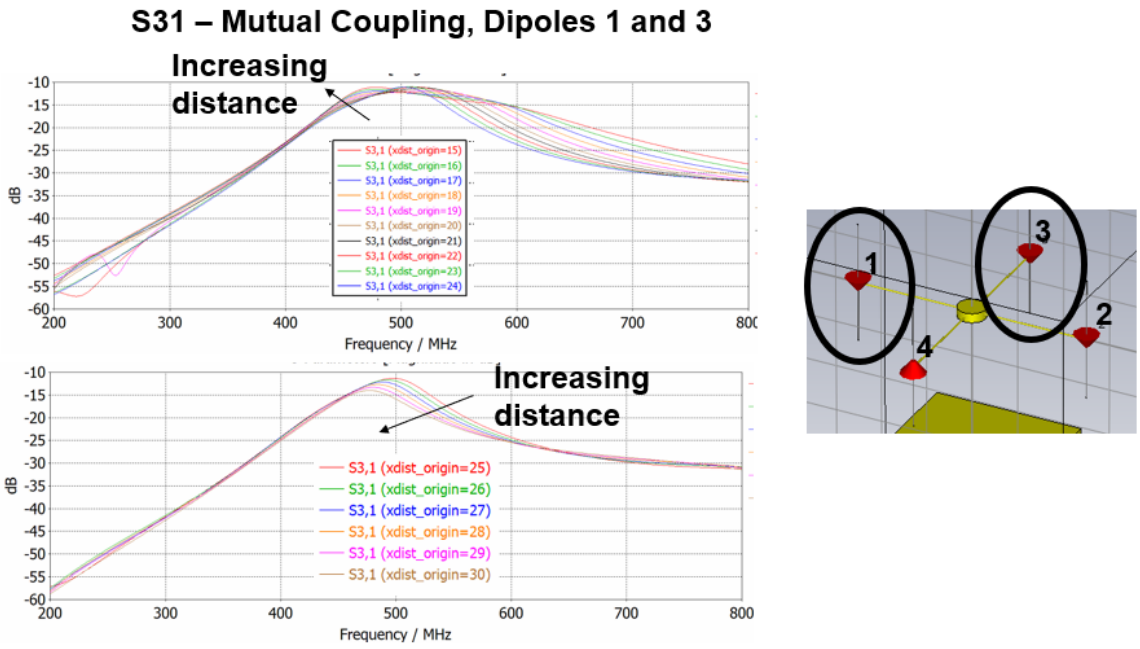

Figure 4.11: Mutual coupling between nearest neighbors (S31) for varying antenna spacing.

remains in the -10 dB to -15 dB range at worst and in the -55 dB to -60 dB range at best.

Finally, we simulated the mutual coupling between antennas across the array, i.e. between antennas 1 and 2 (S21). In Fig 4.12, we see generally worse mutual coupling as we increase the antenna spacing distance. However, S21 remains below -15 dB in the worst case for all antenna spacing distances.

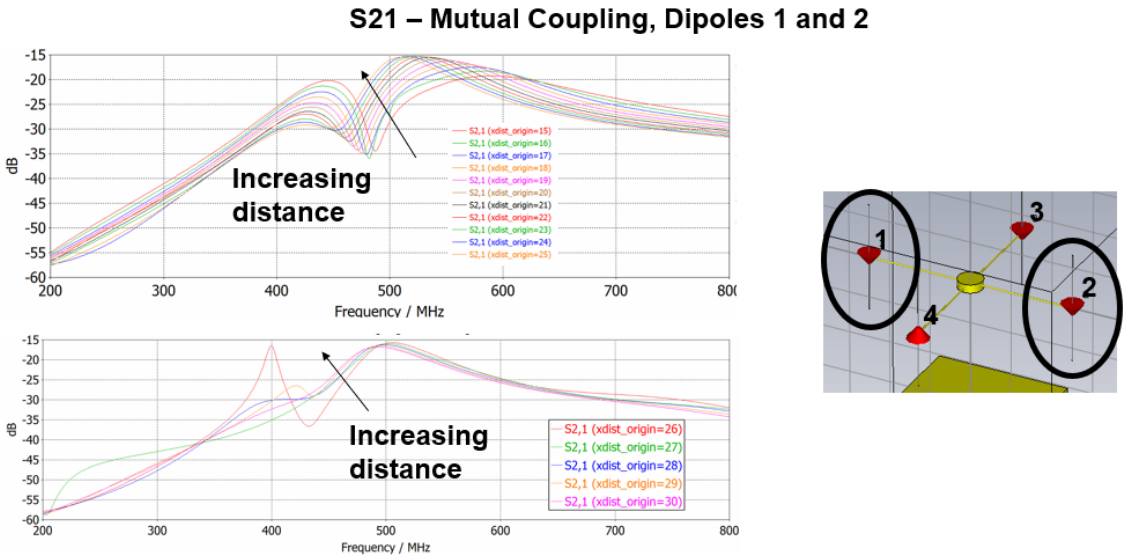

Figure 4.12: Mutual coupling between non-nearest neighbors (S21) for varying antenna spacing.

Based on the S-parameters for the varying distances, we opted to use d = 27 cm, which gives the best return loss, thus coupling the most power into free space. While this may not be the most ideal in terms of mutual coupling, S21 and S31 are both below -12 dB for this value.

4.3 Final Antenna Array Design: Narrow Fiberglass Cross-Frame

In summary, we found the antenna array had a more ideal beam pattern if we oriented the antennas vertically, rather than at 45°. This lessened the effect that the metal electronics box had on the main beam lobe. In addition, we found that using narrow fiberglass tubes rather than a copper throwing star to mechanically support the antenna array made the beam

pattern more regular. Finally, we inserted a balun that electrically separated the antenna from any conductive components in the mechanical frame. Fig. 4.13 shows a summary of the main changes, and the final antenna design is depicted in Fig. 4.14.

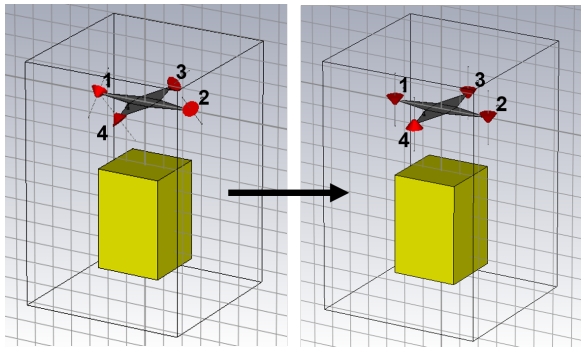

(a)

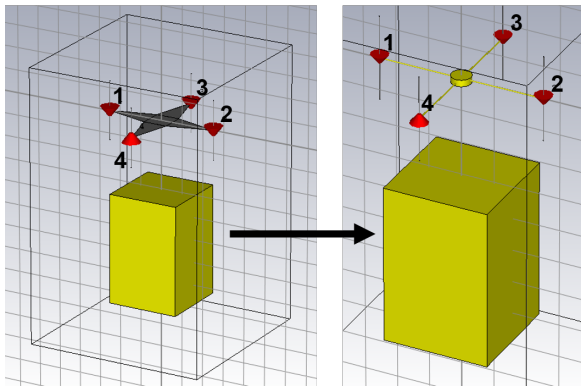

(b)

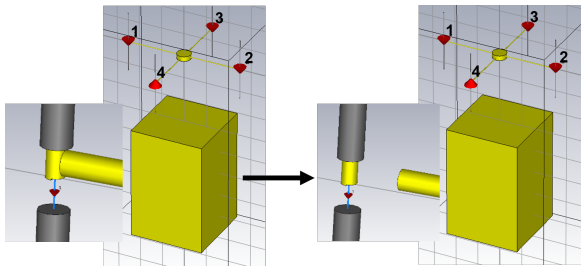

(c)

Figure 4.13: (a) Initial tilted 45° antenna orientation and final vertical antenna orientation, (b) Initial throwing star antenna configuration and final thin cross frame configuration, and (c) Initial antenna setup with no balun and final antenna setup with balun.

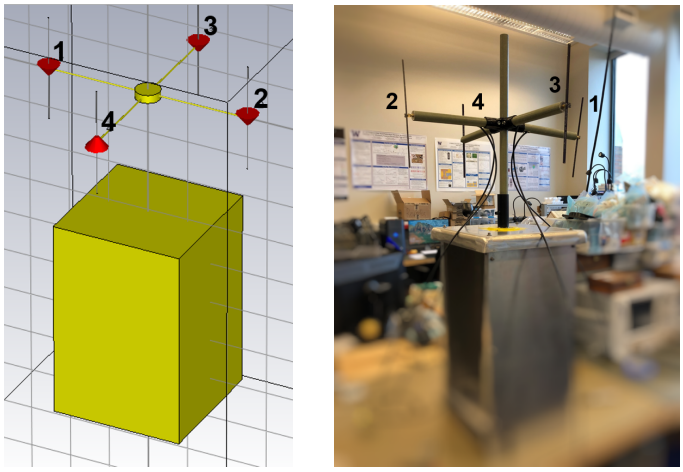

(a) (b)

Figure 4.14: Final antenna design and setup in (a) CST and (b) lab environment. The final design has vertically oriented dipoles, thin fiberglass tubing for mechanical support, PCB antennas with a balun, and a center-to-dipole length of 27 cm.

A comparison of the simulated and measured S-parameter results for the initial and final antenna designs are shown in Fig. 4.15 and Fig. 4.16, respectively. In the initial setup, S21, S31, and S41 were greater than -25 dB across most of the 200-800 MHz spectrum.

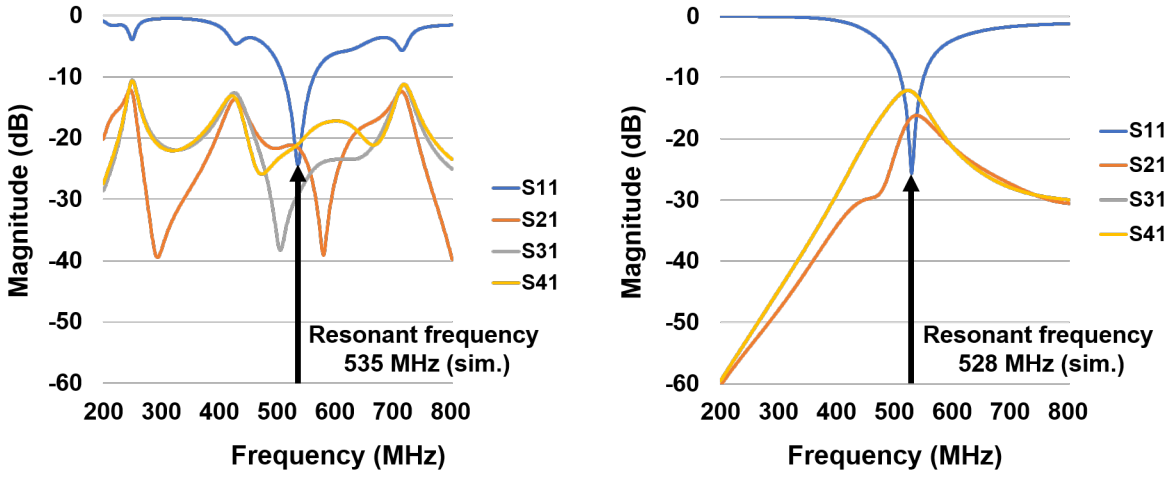

(a) (b)

Figure 4.15: Simulated S-parameters for (a) initial and (b) final antenna setup.

In the final design, they only reached -25 dB in the 450-650 MHz range, and were equal to or less than -30 dB in the remainder of the spectrum. Mutual coupling reached a peak around the resonant frequency at a magnitude of approximately -12 dB in the simulated setup and -15 dB in the experimental setup.

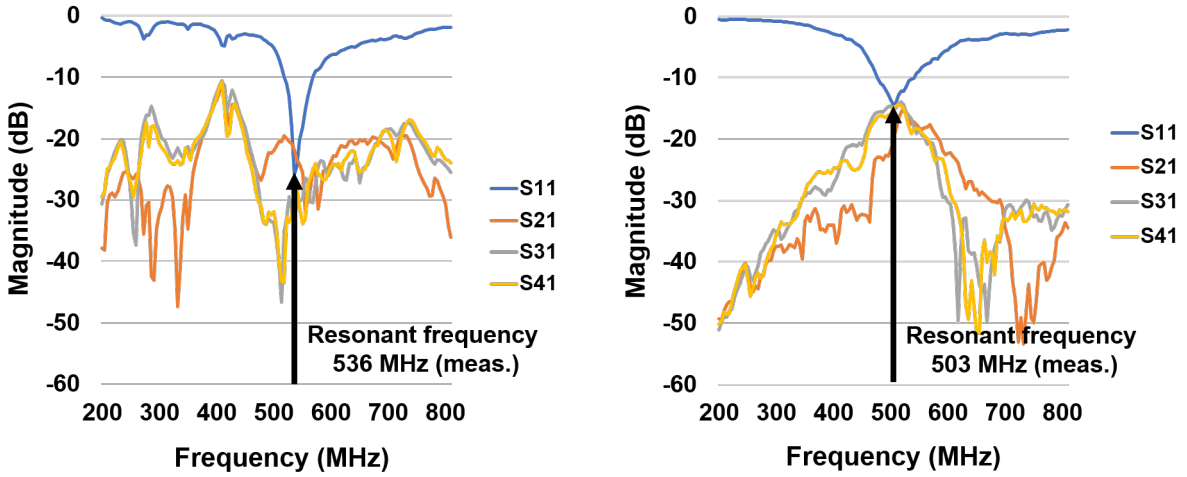

Figure 4.16: Measured S-parameters for (a) initial and (b) final antenna setup.

The far-field beam patterns also show considerable improvement from initial to final design. For the initial design, the beam pattern was not uniform, experiencing strong mutual coupling from the electronics box with the dipoles at a 45° angle. In the final design, the pattern was fairly uniform, with radiated power at a minimum directly above and below the antenna array, which is what we would expect for vertically-oriented dipoles. The vertical orientation lessened the electronics box effect on the beam pattern. A comparison of the far-field beam patterns for the initial and final antenna designs is shown in Fig. 4.17.

4.4 Over-The-Air (OTA) Measurements

To verify an over-the-air (OTA) data capture with the final antenna array, we performed an outdoor test. Setting the antenna array up in a location with a direct line of sight to the digital television (DTV) transmitters, we used a FieldFox Handheld RF and Microwave

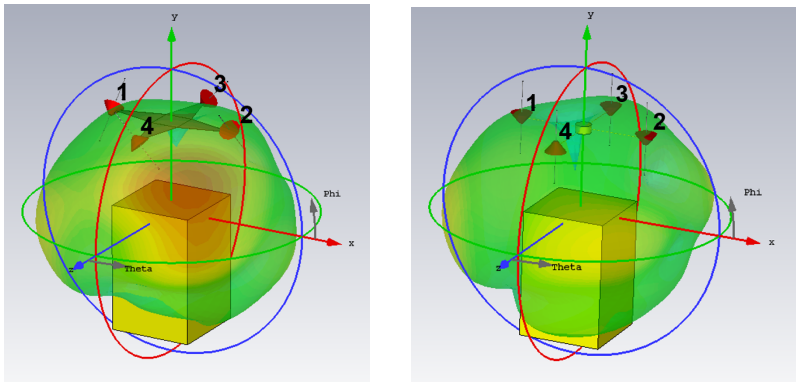

(a) (b)

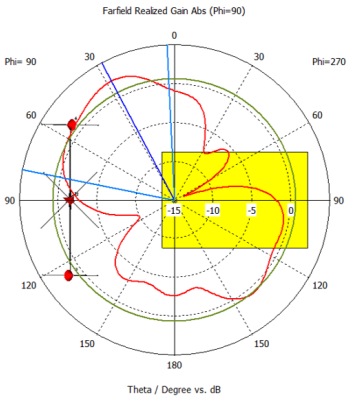

(c)

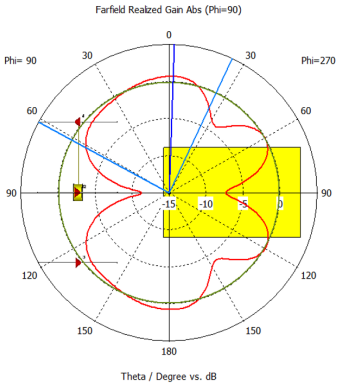

(d)

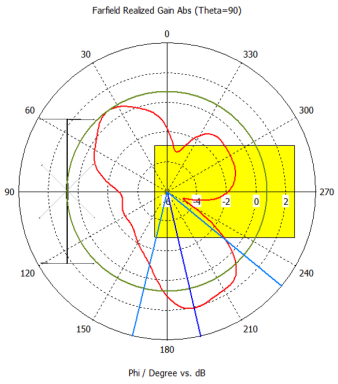

(e)

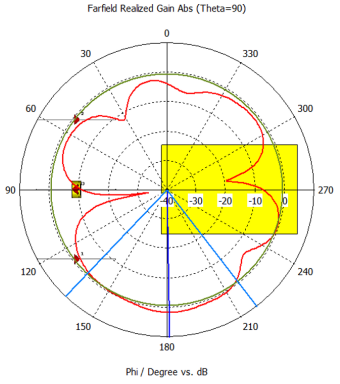

(f)

Figure 4.17: 3D far-field realized gain for (a) initial and (b) final antenna setup. Polar far-field realized gain with phi=90° for (c) initial and (d) final antenna setup. Polar far-field realized gain with theta=90° for (a) initial and (b) final antenna setup.

Analyzer to process the captured signals. Fig. 4.18 shows the measured frequency spectrum of one channel in the DTV band, and Fig. 4.19 displays the measured OTA S-parameters.

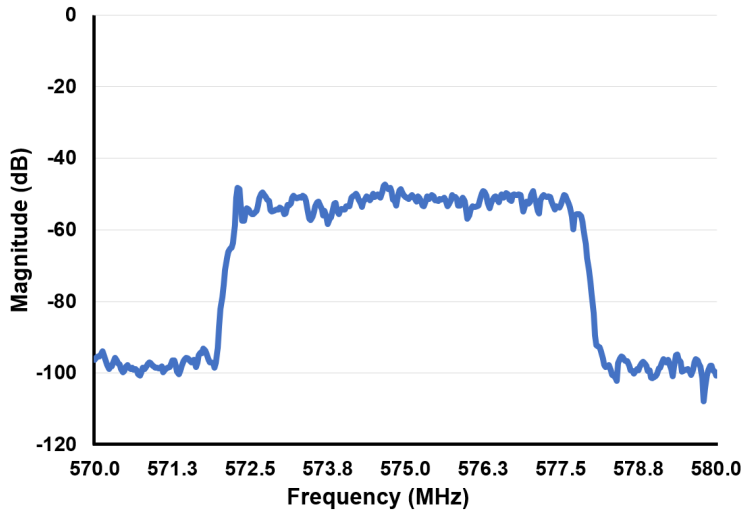

Figure 4.18: Measured frequency spectrum of one DTV channel in the over-the-air (OTA) antenna test.

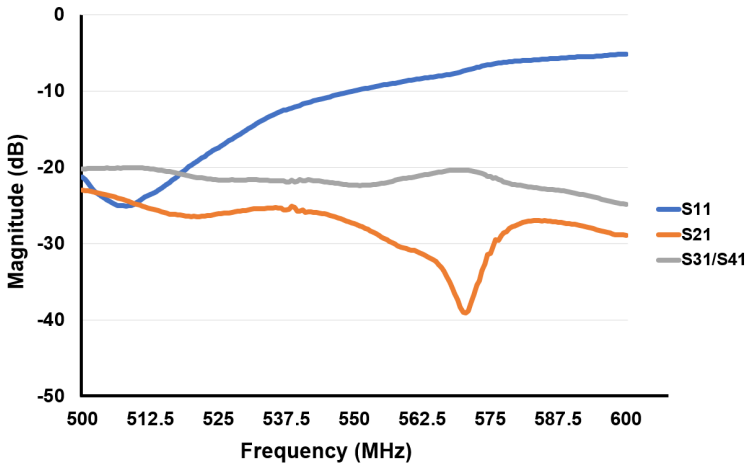

Figure 4.19: Measured S-parameters in over-the-air (OTA) antenna test.

Chapter 5

DIRECT SAMPLING DIGITAL RECEIVER

With the functional ZeroScatter tag and finalized dipole antenna elements, we developed a direct sampling digital receiver designed to capture and process ZeroScatter sensor data. The receiver boards used in the following experiments were the Texas Instruments (TI) ADC32RF45 ADC Evaluation Module (EVM) and the TSW14J56 Evaluation Module (EVM). The TSW14J56 EVM is accompanied by the High Speed Data Converter (HSDC) Pro Graphic User Interface, and the complete system captures and evaluates data samples from the ADC EVM. We developed a short program to process the HSDC captured data in MATLAB. For our application, we set up the digital receiver with an input clock frequency of 2.9 Gsps. The corresponding resolution of the receiver's analog-to-digital converter (ADC) at that input frequency is 14 bits, the dynamic range, or effective number of bits (ENOB), is 9 bits, and the spurious free dynamic range (SFDR) is 58 dBc.

We performed two tests with the BPSK ZeroScatter system, each implementing a different source to provide the carrier signal. One experimental setup used a 550 MHz continuous wave (CW) signal from an Agilent signal generator, and the other was a complete ambient backscatter system, using ambient digital television (DTV) signals received by our dipole antenna elements as the carrier source. In both setups, captures from the digital receiver show successful backscatter transmission of sensor data from the BPSK ZeroScatter tag. The results of both experiments will be discussed in this section.

5.1 Digital Receiver Hardware and Setup

The ADC32RF45 Evaluation Module (EVM) demonstrates the performance of a dual 2.9-Gsps 14-bit analog-to-digital converter (ADC) with external clocking. The EVM includes

the ADC32RF45 device, and external clocking is provided by an Agilent signal generator supplying a 2.9 GHz signal. The Texas Instruments (TI) TSW14J56 Evaluation Module (EVM) is a pattern generator and data capture card used to evaluate performances of the TI family of high-speed ADCs. The receiver hardware and setup is shown in Fig. 5.1, and a break down of the internal receiver components and receiver setup is shown in the block diagram of Fig. 5.2.

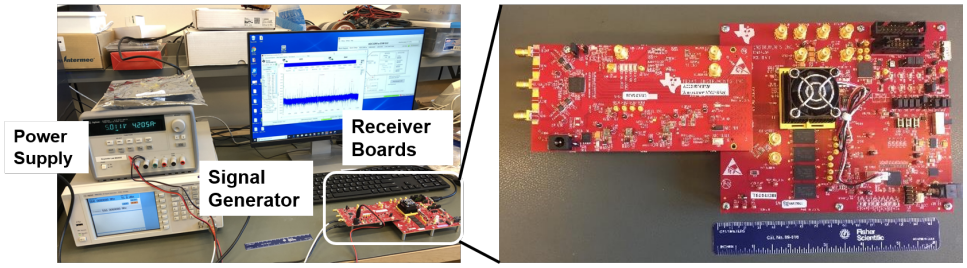

Figure 5.1: Photo of receiver hardware setup.

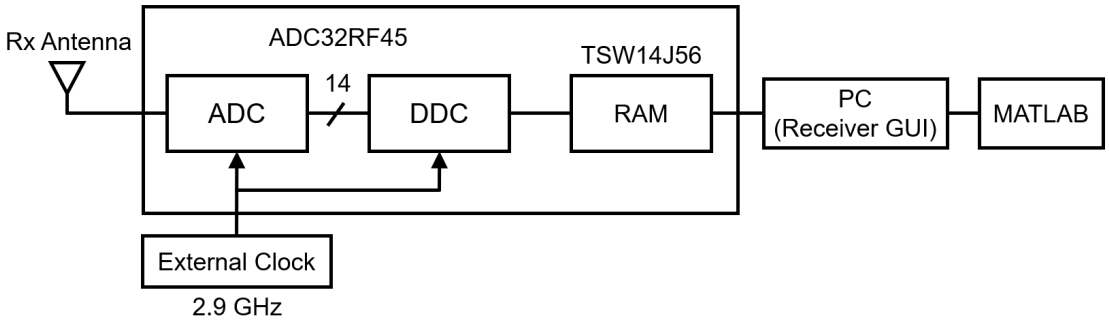

Figure 5.2: Block diagram of receiver hardware setup and internal receiver components.

5.1.1 Implementation of internal digital downconverter (DDC) on the ADC32RF45 EVM for enhanced capture resolution

Because the BPSK data stream from the ZeroScatter tag is being sent at a rate of 9.4 kbps, we would expect to see 9.4 kHz subcarriers in the received backscattered signal, along with the 550 MHz carrier. To improve capture resolution for the relatively small frequency

subcarriers, we implemented the internal digital downconverter (DDC) on the ADC32RF45 EVM. The DDC decimation reduces the sample rate of the signal by removing samples from the data stream. The decimation factor divides the specified sampling rate (clock frequency) to determine the actual sampling rate used by the ADC.

Our experimental DDC setup in the EVM software is depicted in Fig. 5.3. Using an Numerically Controller Oscillator (NCO) frequency of 549 MHz, the DDC maps the 550 MHz carrier frequency to 1 MHz in the down-converted spectrum. Upon testing, the internal clock option on the DDC appeared to be much noisier than the external clock, so we completed the experiments with an external clock supplied by a signal generator set at 2949.12 MHz. Given a decimation factor of 16, the actual ADC data rate was 184.32 MHz. With a total of 67,108,864 samples per capture, the total capture is approximately 0.364 seconds.

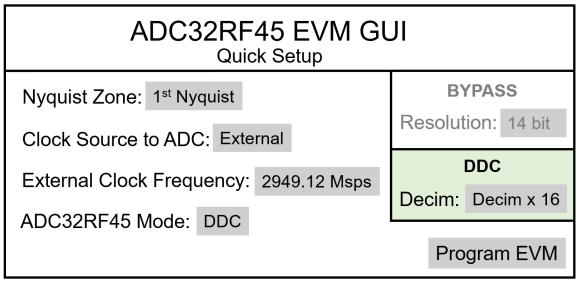

(a)

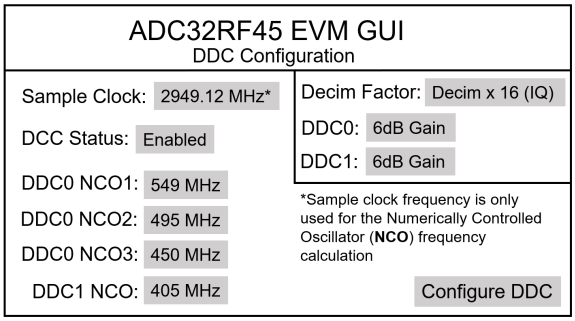

(b)

Figure 5.3: (a) ADC32RF45 Evaluation Module (EVM) GUI setup for the ZeroScatter tag capture. (b) EVM GUI setup for the digital downconverter (DDC) on the ADC32RF45 EVM.

5.2 Testing of ZeroScatter Tag with 550 MHz Continuous Wave (CW) Carrier

The experimental setup with the CW carrier consisted of a signal generator providing a 550 MHz signal in the DTV band, the BPSK ZeroScatter tag connected to a dipole antenna element (resonant at 550 MHz), and a receiving dipole antenna element (resonant at 550 MHz) connected to the receiver board via coaxial cable. The antennas used are identical to the dipoles from the final antenna array described in Chapter 4. The digital receiver was powered by a 5V power supply and connected to the PC via USB for access to the HSDC GUI. Fig. 5.4 shows a block diagram and photo of the experimental setup.

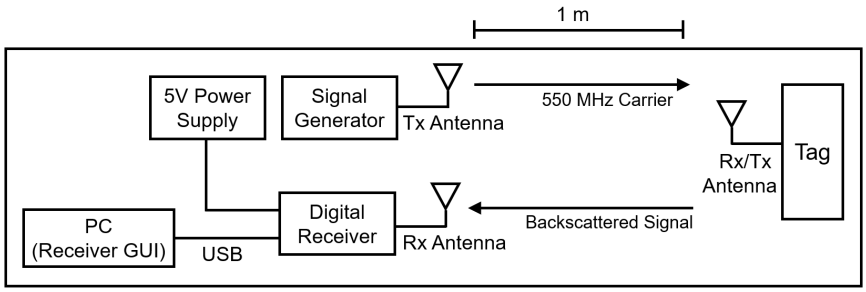

(a)

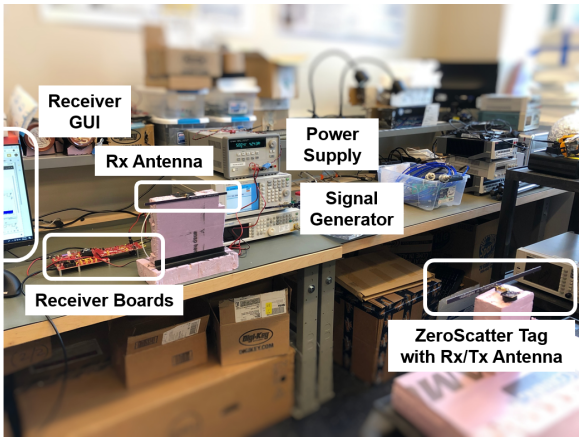

(b)

Figure 5.4: (a) Block diagram of the experimental setup with a supplied 550 MHz carrier source (b) Photo of the experimental setup.

In this setup, the ZeroScatter tag uses the 550 MHz signal from the signal generator as a carrier to backscatter the temperature sensor data from the PIC12LF1552 microcontroller. The ZeroScatter tag, designed and programmed in BPSK mode, toggles between input and output modes on one of the PICs I/O pins to send data in 32-bit (4-byte) packets, consisting of a header (0x55), temperature data, tag ID (0xAD), and CRC-8 checksum. The receiving antenna and digital receiver are positioned to capture the backscattered data from the tag.

(a)

(b)

Figure 5.5: High Speed Data Converter (HSDC) GUI capture with (a) ZeroScatter tag absent and (b) ZeroScatter tag present, showing the backscattered ZeroScatter signal.

The TI High Speed Data Converter (HSDC) Pro GUI allows us to view and process the received signals. Fig. 5.5 (b) is a screenshot of the HSDC capture of the ZeroScatter data, with Fig. 5.5 (a) providing a capture comparison when the tag is not present. The 550 MHz signal, downconverted to 1 MHz, is visible and the smaller peaks to the left and right of the carrier represent the frequency of the ZeroScatter data.

5.2.1 Post-processing of ZeroScatter capture with the digital receiver

The MATLAB spectrogram plots in Fig. 5.6 show the captured receiver data when the ZeroScatter tag is present versus absent. When the tag is present, depicted in Fig. 5.6 (b), the frequencies of the backscattered signal are visible to the top and bottom of the strong downconverted carrier frequency.

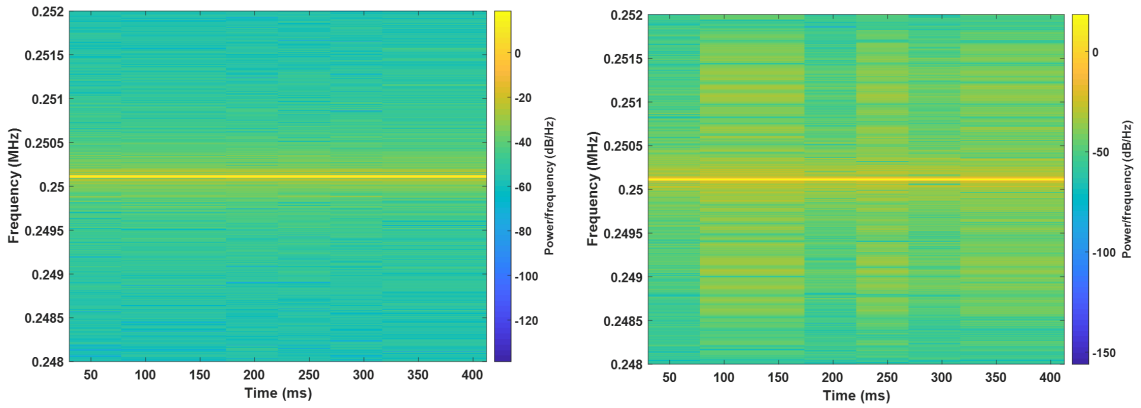

Figure 5.6: Spectrogram plots of the captured receiver data with (a) ZeroScatter tag absent and (b) ZeroScatter tag present, showing the backscattered ZeroScatter signal.

After performing a pspectrum function on the captured signal in MATLAB, we can see the ZeroScatter data. The 32-bit packets are shown in Fig. 5.7 (a) and the individual bits in (b). The header (0b01010101), temperature data (0b00010000), tag ID (0b10101101), and CRC checksum (0b01100101) btyes are all visible.

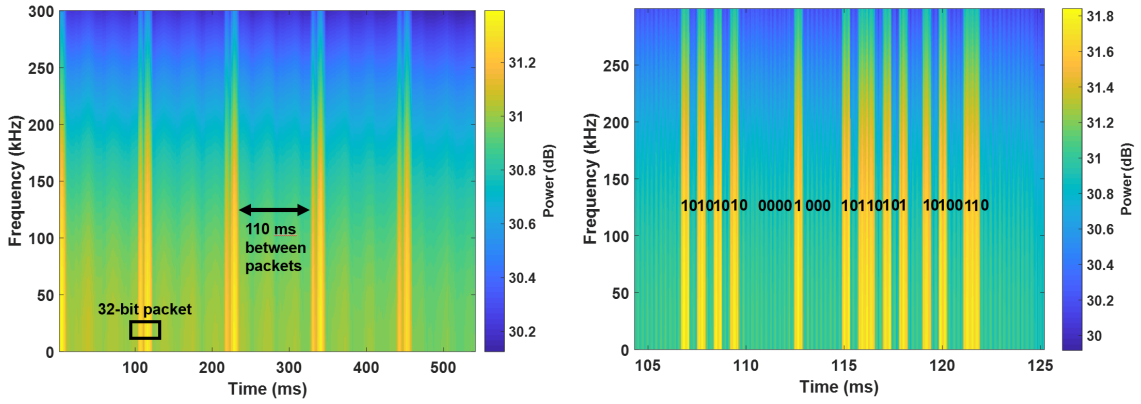

(a) (b)

Figure 5.7: Pspectrum plots of the captured receiver data showing the (a) 32-bit packets (b) individual data bits.

As depicted in Fig. 5.8, the ZeroScatter bit stream captured by the digital receiver is identical to that from the over-the-air oscilloscope capture presented in Chapter 3, as the internal temperature readings from the PIC sensor were the same for the two captures.

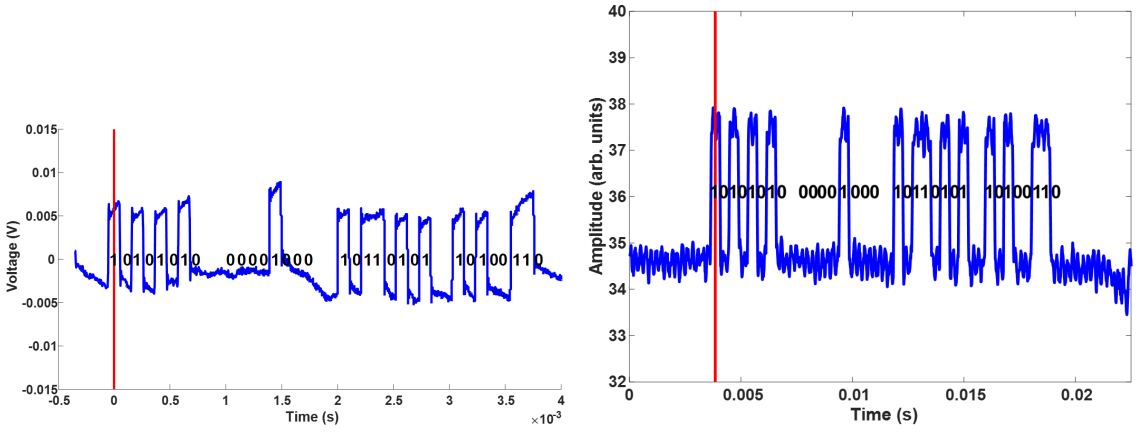

(a) (b)

Figure 5.8: Comparison of (a) ZeroScatter data from the over-the-air oscilloscope capture reproduced from Chapter 3 and (b) ZeroScatter data from direct sampling digital receiver capture.

5.3 Testing of ZeroScatter Tag with Ambient Digital Television (DTV) Carrier

In our complete ambient backscatter system, the dipole antenna elements from the antenna array discussed in Chapter 4 were used to capture ambient DTV signals from the environment, and these signals provided the carrier signal for the ZeroScatter transmission. A block diagram of the ambient carrier setup is shown in Fig. 5.9. The setup consisted of the BPSK ZeroScatter tag connected to a dipole antenna element (resonant at 550 MHz) designed to capture ambient DTV signals from the TV tower. A receiving dipole antenna element (resonant at 550 MHz) designed to capture the backscattered ZeroScatter sensor data was connected to the receiver board via coaxial cable. The digital receiver was powered by a 5V power supply and connected to the PC via USB for access to the HSDC GUI. Other than the change in carrier source, our ambient setup is identical to the continuous wave carrier setup shown in Fig. 5.4.

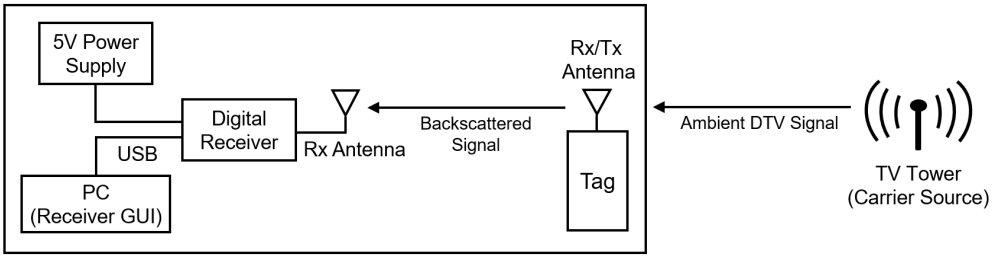

Figure 5.9: Block diagram of the ambient ZeroScatter experimental setup.

The MATLAB spectrogram plots in Fig. 5.10 show the captured receiver data when the ZeroScatter tag is present versus absent. When the tag is present, depicted in Fig. 5.10 (b), the frequency of the backscattered signal is visible at approximately 7.495 MHz. After performing a pspectrum function on the captured signal, we can see the ZeroScatter data. The individual bits within a 32-bit packet are shown in Fig. 5.11 (a). Taking one row from (a), we can see the individual bits on an amplitude vs. time plot in Fig. 5.11 (b). Reading the bytes from right to left, as the bits were sent least significant bit first, the header (0b01010101),

temperature data (0b00001100), tag ID (0b10101101), and CRC checksum (0b10100110) bytes are all visible. The temperature value 0x0C corresponds to a temperature of 12 °C or 53.6 °F, which is reasonable for an outdoor capture. The CRC checksum for bytes 0x55, 0x0C, and 0xAD was confirmed as 0xA6 with an online CRC calculator.

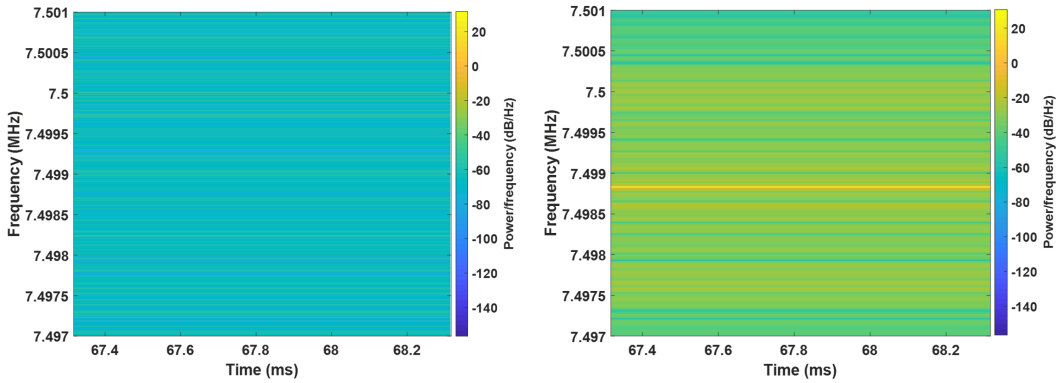

(a) (b)

Figure 5.10: Spectrogram plots of the over-the-air captured receiver data with (a) ZeroScatter tag absent and (b) ZeroScatter tag present, showing the backscattered ZeroScatter signal.

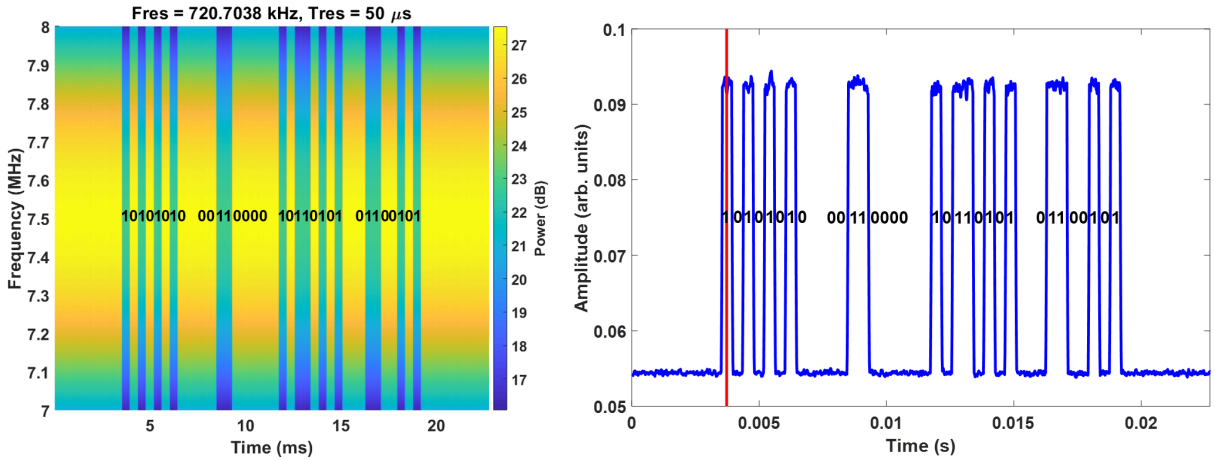

(a) (b)

Figure 5.11: Pspectrum plot of the over-the-air captured receiver data showing the individual data bits and (b) Amplitude vs. time plot of ZeroScatter data.

Chapter 6

CONCLUSION

This thesis describes ZeroScatter, an approach for using billions of existing digital I/O pins as backscatter modulators. ZeroScatter leverages the surprising fact that low-speed digital I/O pins on commodity digital devices such as MCUs and FPGAs can be re-purposed as PSK backscatter modulators in the UHF and microwave bands, even though their digital toggle frequencies are limited to much lower frequencies. We demonstrate that the ZeroScatter approach can be used to provide BPSK data uplinks with zero added components, and QPSK data uplinks with only two added capacitors.

We present measured data from a BPSK ZeroScatter backscatter sensor tag having only two components: a digital I/O pin of a PIC12LF1552 8-bit microcontroller that costs less than $0.50 USD, and a 3 V lithium coin cell battery. The prototype ZeroScatter tag performs BPSK backscatter modulation of an incident 915 MHz carrier with 32-bit packets containing a tag unique-ID, an on-chip temperature reading, and a cyclic redundancy code (CRC) checksum. At a data rate of 9.4 kbps and a carrier power of +10 dBm, a range exceeding 3 m is demonstrated in an ordinary office hallway. In active operation, the ZeroScatter tag consumes only 628 μA at 3.0 V or 473 μA at 1.8 V. We also present measured data from a QPSK ZeroScatter tag using two digital I/O pins to provide four distinct symbol states in a QPSK constellation, using two added capacitors to separate the symbol states. A symbol rate of 18 ksymbols/s and a data rate of 36 kbps is demonstrated.

Using the BPSK ZeroScatter tag, we present a complete ambient backscatter system, including PCB-fabricated dipole antenna elements and a direct sampling digital receiver, that leverages ambient digital television (DTV) signals in the 500-600 MHz band as a carrier source. A 4-dipole antenna array initially designed by our collaborators for a passive radar

application was tested and optimized in this work, and the individual dipole elements were implemented as transmitting and receiving antennas in the ambient ZeroScatter system. The direct sampling digital receiver, composed of the Texas Instruments ADC32RF45 EVM and TSW14J56 EVM, captured and processed the backscattered sensor data from the ZeroScatter tag. In both the 550 MHz continuous wave (CW) carrier setup and the ambient carrier setup, the ZeroScatter transmission was visible, showing internal temperature readings of 60.8 °F and 53.6 °F, respectively.

Future work with the ZeroScatter tag includes refinement of the QPSK constellation via more careful tuning of the added impedances to improve the symmetry of the constellation. Additional future work includes the demonstration of QAM backscatter [2] using three or more digital I/O pins to form eight or more points in a higher-order QAM constellation, and the development of higher data rate ZeroScatter links using digital logic in an FPGA as the data source. Future work with the antenna array and direct sampling digital receiver includes demodulating the ambient carrier or array processing to find the angle to the ZeroScatter tag. With multiple receivers, it would be possible to determine the location of the ZeroScatter tag in a 2-D plane. Simultaneously processing different DTV transmitters at different locations would be another method of locating the tag that could be explored in future work.

BIBLIOGRAPHY

[1] H. Stockman, "Communication by Means of Reflected Power," Proc. of the IRE, vol. 36, no. 10, pp. 1196-1204, Oct. 1948.

[2] S. Thomas, E. Wheeler, J. Teizer and M. Reynolds, "Quadrature Amplitude Modulated Backscatter in Passive and Semipassive UHF RFID Systems," IEEE Trans. Microw. Theory Techn., vol. 60, no. 4, pp. 1175-1182, April 2012.

[3] S. Thomas and M. Reynolds, "A 96 Mbit/sec, 15.5pJ/bit 16-QAM Modulator for UHF Backscatter Communication", in Proc. IEEE RFID 2012, Orlando, FL, April 3-5, 2012, pp. 185-190.

[4] R. Correia, A. Boaventura and N. Borges Carvalho, "Quadrature Amplitude Backscatter Modulator for Passive Wireless Sensors in IoT Applications," IEEE Trans. Microw. Theory Techn., vol. 65, no. 4, pp. 1103-1110, April 2017.

[5] J. Ensworth and M. Reynolds, "Every smart phone is a backscatter reader: Modulated backscatter compatibility with Bluetooth 4.0 Low Energy (BLE) devices," in Proc. 2015 IEEE Intl. Conf. on RFID (RFID), San Diego, CA, pp. 78-85, 2015.

[6] J. Ensworth and M. Reynolds, "BLE-Backscatter: Ultra-low-power IoT nodes compatible with Bluetooth 4.0 Low Energy (BLE) smartphones and tablets", IEEE Trans. Microw. Theory Techn., vol. 65, no. 9, pp. 3360-3368, 2017.

[7] B. Kellogg, V. Talla, S. Gollakota, J. Smith, "Passive Wi-Fi: Bringing Low Power to Wi-Fi Transmissions", in Proc. Usenix Symp. on Networked Syst. Design and Implementation (NSDI), 2016.

[8] A. Sample, D. Yeager, P. Powledge, A. Mamishev, and J.R. Smith, "Design of an RFID-Based Battery-Free Programmable Sensing Platform," IEEE Trans. on Instrum. and Meas., vol. 57, no. 11, pp. 2608-2615, 2008.

[9] C. Carrender, "Full-spectrum passive communication system and method," United States Patent 6970089B2, Nov. 29, 2005.

[10] D. Yeager, A. Sample, J.R. Smith, "Ambient Backscatter: Wireless Communication out of Thin Air," ACM SIGCOMM Computer Communication Review., vol. 43, no. 4, pp. 39-50, 2013.

[11] G. Wang, F. Gao, R. Fan, and C. Tellambra, "Ambient Backscatter Communication Systems: Detection and Performance Analysis," IEEE Trans. on Comm., vol. 64, no. 11, pp. 4836-4846, 2016.

[12] D. Darsena, G. Gelli, and F. Verde, "Modeling and Performance Analysis of Wireless Networks With Ambient Backscatter Devices," IEEE Trans. on Comm., vol. 65, no. 4, pp. 1797-1814, 2017.

[13] D. Hoang, D. Niyato, P. Wang, D.I. Kim, and Z. Han, "Ambient Backscatter: A New Approach to Improve Network Performance for RF-Powered Cognitive Radio Networks," IEEE Trans. on Comm., vol. 65, no. 9, pp. 3659-3674, 2017.

[14] A. Dadkhah, J. Rosenthal, M. Reynolds, "ZeroScatter: Zero-Added-Component Backscatter Communication using Existing Digital I/O Pins," in 2019 IEEE Topical Conf. on Wireless Sensors and Sensor Netw. (WiSNet), Jan 2019.

[15] A. Sample, D. Yeager, P. Powledge, and J. Smith, "Design of a passively-powered, programmable sensing platform for UHF RFID systems," in 2007 IEEE Intl. Conf. on RFID, March 2007, pp. 149-156.

[16] A. Sharma, E. Kampianakis, J. Rosenthal, A. Pike, A. Dadkhah, and M. Reynolds, "Wideband UHF DQPSK Backscatter Communication in Reverberant Cavity Animal Cage Environments," IEEE Trans. Antennas Propag., vol. PP, pp. 1-10, 2019.

[17] W. Sun, J.D. Sahr, and T. Goodson, "Digital demodulation of DTV signals for passive radar application," in 2016 IEEE Radar Conference (RadarConf), May 2016.

[18] W. Barott and J. Engle, "Single-antenna ATSC passive radar observations with remodulation and keystone formatting," in 2014 IEEE Radar Conference (RadarConf), May 2014.